



# True Triaxial Experimental Study on the Variation Characteristics of Rockburst with the Number of Fast Unloading Surfaces

Jieyu Li<sup>1,2</sup> · Dongqiao Liu<sup>1</sup> · Manchao He<sup>1</sup> · Yunpeng Guo<sup>1</sup>

Received: 24 August 2022 / Accepted: 16 March 2023 / Published online: 5 May 2023  
© The Author(s), under exclusive licence to Springer-Verlag GmbH Austria, part of Springer Nature 2023

## Abstract

The fast unloading delayed rockburst experiments on single-side, double-side, three-side, and four-side were carried out using the self-developed true triaxial rockburst experimental apparatus, which can realize the fast unloading of multiple loading surfaces in the horizontal direction under high stress. The rockburst experiment's stress–strain curve, energy evolution, failure characteristics, and acoustic emission (AE) characteristics are investigated. The results show that the rockburst gradually reduces the axial peak stress and strain when increasing the number of unloading surfaces (NUS). The rise in the axial strain at the fast unloading point will progressively grow when the NUS increases, indicating that the sample's expansion in the unloading direction will gradually increase. Fast unloading causes unloading damage, which causes a sudden rise in dissipated energy at the unloading point. The total energy and elastic strain energy input by axial stress at the bursting point gradually declines when the NUS increases, but the dissipated energy increases. The release rate of elastic strain energy at the bursting point increases when the NUS increases, and the rockburst becomes more intense. The abrupt value of the cumulative AE hits at the fast unloading point and the cumulative AE hits at the burst point increase with the NUS increase. The changing trend of the multifractal parameter, which initially decreases and then rises abruptly, can be regarded as the precursor of rockburst. The hysteresis of the precursor of rockburst grows when the NUS increases.

## Highlights

- The fast unloading delayed rockburst tests on single-side, double-side, three-side, and four-side were carried out using the self-developed true triaxial rockburst experimental apparatus.
- Energy analysis and high-speed recording of the rockburst process found that the severity of the rockburst does not depend on the amount of elastic strain energy stored in the rock sample but rather on the release rate of energy at the rockburst point.
- The changing trend of the multifractal parameter, which initially decreases and then rises abruptly, can be regarded as the precursor of rockburst. The hysteresis of the precursor of rockburst grows when the NUS increases.

**Keywords** Delayed rockburst experiment · Fast unloading · Energy evolution · Acoustic emission (AE) multifractal

✉ Dongqiao Liu  
liudongqiao@yeah.net

✉ Manchao He  
hemanchao@263.net

<sup>1</sup> State Key Laboratory for GeoMechanics and Deep Underground Engineering, China University of Mining and Technology, Beijing 100083, China

<sup>2</sup> Norman B. Keevil Institute of Mining Engineering, University of British Columbia, Vancouver, BC V6T 1Z4, Canada

## 1 Introduction

With the development of rock engineering to the depth, the initial in-situ stress of excavated rock mass gradually increases. The stress concentration of surrounding rock caused by engineering excavation is more pronounced, which leads to the increasingly prominent problem of rockburst (He et al. 2018). A rockburst seriously affects the life safety of construction personnel and the regular operation

of engineering equipment and is among the most dangerous disasters in rock engineering. With the increasingly prominent problem of rockburst, many rock mechanics researchers have carried out much research on rockburst (Ortlepp and Stacey 1994; Kaiser et al. 2001; Wang and Park 2001; Stacey 2016; Feng et al. 2017; Si and Gong 2020). However, unfortunately, the mechanism of rockburst is still an unsolved problem. With the true triaxial instrument development, the research on rockburst simulation experiments has gradually increased. Through the true triaxial equipment to simulate the rockburst experiment with an engineering background, reproduce the rockburst phenomenon indoors, and obtain a large number of the rockburst evolution data through various advanced monitoring equipment, to make the research of rockburst more transparent and concise, which is critical in revealing the rockburst mechanism.

With the deepening of people's understanding of rockburst, rockburst simulation equipment and experiments are constantly updated and developed. Since Cook (1963) used a uniaxial compression experiment to explore pillar rockburst, many scholars have conducted many uniaxial compression rock mechanics experiments to simulate rockburst (Zhang et al. 2020; Wang et al. 2020; Gong et al. 2022). The uniaxial compression rockburst simulation test adopts the oil pressure control system. When the load reaches the peak point, the unloading is caused by the slow oil supply speed of the oil circuit, and it is challenging to realize the simulation of the rockburst throwing phenomenon. Gu et al. (2014) used a combination of spring and loading systems to simulate a rockburst. The spring can store energy to supplement the unloading of the hydraulic system at the peak point. Fakhimi et al. (2016) designed a mild steel frame to simulate the roof structure in the mining system and combined it with the loading equipment to simulate the pillar rockburst. In the biaxial compression test, Steif (1984) carried out a biaxial compression rockburst test and studied the law of rock crack growth under stress loading. Zhang et al. (2017) also conducted biaxial compression rockburst simulation experiments to study the dominant frequency characteristics of AE from rockburst. Uniaxial and biaxial compression tests cannot simulate excavation unloading, while the unloading effect of deep high-stress rock mass will be more serious. To fully consider the impact of excavation unloading on rockburst, Cai et al. (2001) studied the energy storage performance and rockburst prediction of deep rock mass in Linglong Gold Mine through conventional triaxial unloading tests. The triaxial stress state of the original rock and the influence of the second principal stress on the rock mass strength during the excavation of deep underground rock mass engineering can't be simulated and studied by conventional triaxial tests. The true triaxial equipment is used to carry out triaxial loading to simulate the rock mass's

initial triaxial stress state. The rapid unloading is used to simulate blasting excavation, which is more consistent with the rock mass stress state transformation in engineering practice. However, the true triaxial loading equipment uses the hydraulic system for loading and unloading. Due to the viscosity of hydraulic oil, it isn't easy to achieve rapid unloading, which is very different from the actual unloading speed of blasting excavation. Aiming at this problem, He et al. (2010, 2012) developed a true triaxial rockburst test equipment that can be quickly unloaded under true triaxial high-pressure loading to form a free face and reproduced the rockburst disaster phenomenon in the process of deep underground chamber excavation indoors, and studied the occurrence process, AE evolution characteristics and rockburst fragments. Akdag et al. (2018) used this rockburst experimental system to carry out the influence of different degrees of thermal damage on the deformation rockburst. Li et al. (2017) carried out the "static stress + dynamic disturbance" rockburst experiment on the wall of a deep, circular cavern. They expounded the dynamic and static combined loading mechanism of different types of rockburst. Su et al. (2019) used the self-developed true triaxial rockburst test system that can realize single-sided rapid unloading and studied the rockburst ejection process and debris ejection velocity with the help of high-speed cameras. Wang et al. (2021) studied the dynamic characteristics of the time-space entropy of rockburst AE by carrying out a true triaxial single-sided rapid unloading granite rockburst experiment. The experimental results provide a new method for rockburst prediction. He et al. (2014) developed a true triaxial impact rockburst experimental system that can apply multiple disturbance waveforms in three loading directions for the rockburst phenomenon induced by rock mass excavation under dynamic load. The energy is analyzed, and the energy discrimination method of impact rockburst is established. Bruning et al. (2018) developed a triaxial loaded hollow cylinder test method to simulate the small rockburst test and study the effect of deviator stress on rockburst characteristics. Das and Singh (2022) simulated tunnel rockburst by developing rock samples with holes, and predicted rockburst by AE. Wibisono et al. (2023) used a mini-tunneling machine to excavate on a true triaxial loaded cube sample to simulate rock burst during tunnel excavation. To sum up, the above rockburst experimental studies are all aimed at the rockburst phenomenon (roadway rockburst) with only one free-face rock structure. However, complex underground rock mass engineering also has roadway intersections with two free faces, three free faces pillars, and four free faces pillars (Esterhuizen et al. 2011). These rock structures with multiple free faces are more likely to produce stress concentration, and the unloading effect is more prominent, leading to rockburst. The excavation method of rock mass in deep underground engineering mainly adopts blasting excavation,

which is a transient unloading process (Lu et al. 2012). Rapid unloading of rock mass under high pressure is bound to cause rapid unloading damage to the rock mass (Xie and He 2004; Qiu et al. 2014). The current rockburst experiment mainly aims at the rockburst phenomenon with one free face. There are few reports on the simulation of rockbursts with multiple free faces and the study of the unloading effect of multiple faces.

This paper uses a new rockburst experiment system to carry out delayed strain rockburst experiments on sandstone with one-sided, double-sided, three-sided, and four-sided rapid unloading. To study the change characteristics of rockburst as the NUS increases. The following chapters analyze the stress–strain, energy evolution, failure process, and AE evolution of the multi-side rapid unloading rockburst experiment. At the same time, the strain, energy, and AE characteristics at the fast unloading point are analyzed emphatically to study the fast unloading effect. This experimental research is of great significance to the unloading effect of rapid unloading of rock mass under high pressure and the rockburst characteristics of rock mass structures with multiple free faces.

## 2 Experimental Procedures

### 2.1 Multi Free Face Rockburst Simulation Method

Figure 1a shows the three-dimensional (3D) stress change state of roadway rockburst surrounding rock unit before and after rock mass excavation. It is in a 3D stress state before excavation, and a free face is generated after the formation of the roadway. The stress perpendicular to the free face becomes zero, and the rock mass unit changes from a 3D six-face stress state to a 3D five-face loading state. As the internal stress near the vertical free face of rock mass decreases to zero with the stress perpendicular to the outside of the free face, the stress perpendicular to the inside of the free face is also in a minimal stress state. Some scholars regard the stress state after roadway excavation as a biaxial compression state (Fan et al. 2018). Figure 1b shows the changing state of 3D stress before and after excavating the intermediate rock mass unit sandwiched by two similar roadways. The rock mass is in the state of 3D stress before excavation. After the two roadways are excavated simultaneously, two free faces are generated, and the stress state is also changed from a 3D stress state to a two-dimensional (2D) stress state. Figure 1c shows the 3D stress change of pillar rock mass structure with three free faces before and after excavation. First, excavate to form a free face, and then excavate two tunnels simultaneously. The rock mass structure in the middle

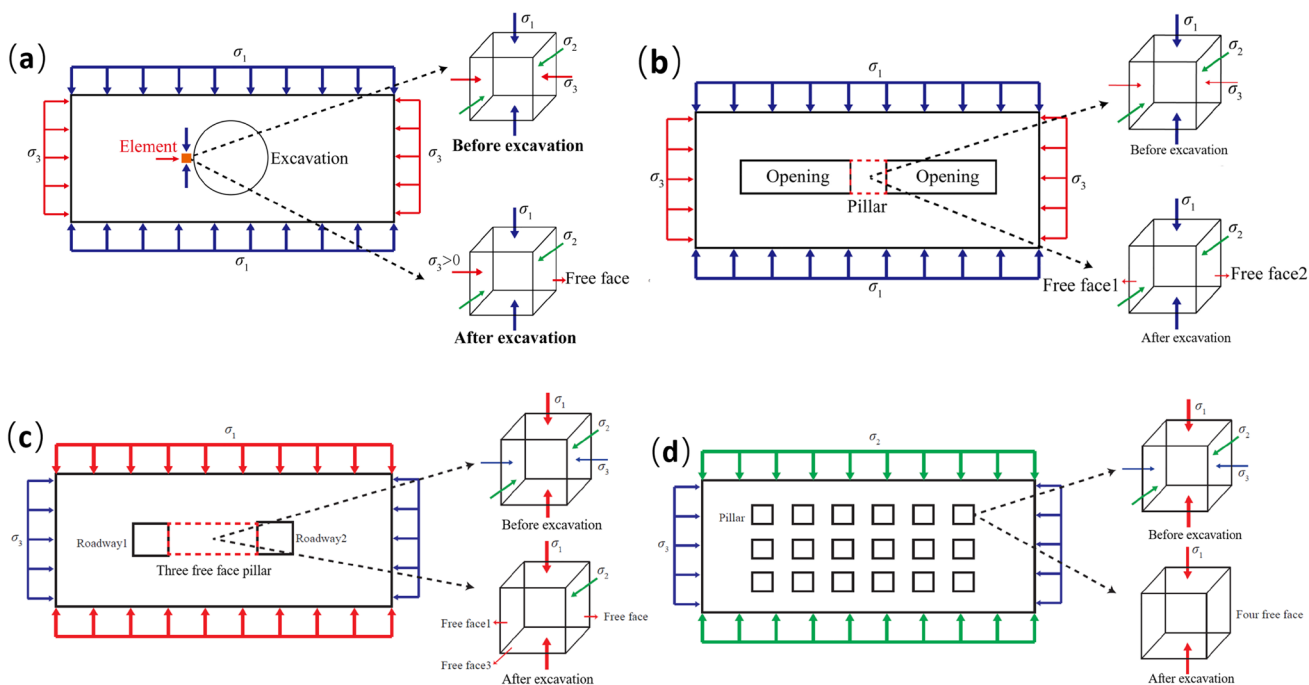


**Fig. 1** Stress transformation diagram of rock mass structure of multiple free faces before and after excavation. **a** Single free surface rock mass structure, **b** double free surfaces, **c** three free surfaces, and **d** four free surfaces

has three free faces, and the stress state changes from 3D stress to axial stress and horizontal stress of one loading surface. Because the stress in the horizontal direction of rock mass element and its relative stress becomes zero, the relative stress in the horizontal direction of rock mass is also in a small state. Figure 1d shows the stress transformation of the pillar rock mass unit with four free faces before and after excavation. Before excavation, the rock mass unit is in the stress loading state of three directions and six faces. After excavation, four free faces are generated in the horizontal direction. The stress state of the rock mass unit changes to a one-way stress state, and the stress in the horizontal direction is zero.

Figure 2 is the true triaxial loading and unloading stress path diagram of the rockburst experiment of multi-face rock structures. Figure 2a shows the stress loading path of single-side fast unloading of rockburst (He et al. 2018). First, the true triaxial 3D stress is loaded to the designed initial stress state of the original rock, and it is kept for some time so that the 3D stress is stably applied to the sample. Then fast unload the stress  $\sigma_{31}$  of a loading surface in the direction of the minimum principal stress  $\sigma_3$  after the end of the holding. Finally, the axial direction stress  $\sigma_1$  is increased until the rockburst occurs. Note: When the loading surface stress  $\sigma_{31}$  is unloaded in the  $\sigma_3$  direction, the relative loading

surface stress  $\sigma_{32}$  decreases to a small value but not zero at the same time. This minor stress is provided by the friction force caused by the loading stress in the other two directions. This small stress corresponds to the minor stress still existing in the rock mass near the free surface of the site. Figure 2b shows the stress loading path of the double-side fast unloading of the rockburst. After the end of the holding load, the stress of the two loading surfaces in the  $\sigma_3$  direction is fast unloading simultaneously. Figure 2c shows the stress loading path of the three-side fast unloading of rockburst. After the end of the keep loading, the stress of the two loading surfaces in the  $\sigma_3$  direction is rapidly unloaded, and then the stress  $\sigma_{21}$  of one loading surface in the  $\sigma_2$  direction is unloaded. The stress  $\sigma_{22}$  of the other loading surface in the same  $\sigma_2$  direction as the single-sided unloading is maintained with smaller stress. Figure 2d shows the stress loading path of the four-side fast unloading of rockburst. After the end of the holding load, the stress of the two loading surfaces in the  $\sigma_3$  direction is quickly unloaded. Then continue to unload the stress of the two loading surfaces in the  $\sigma_2$  direction. After the unloading is completed, increase the axial stress to simulate the stress concentration until the rockburst occurs. The loading initial in-situ stresses  $\sigma_1$ ,  $\sigma_2$ , and  $\sigma_3$  set in this study are 120 MPa, 60 MPa, and 30 MPa,

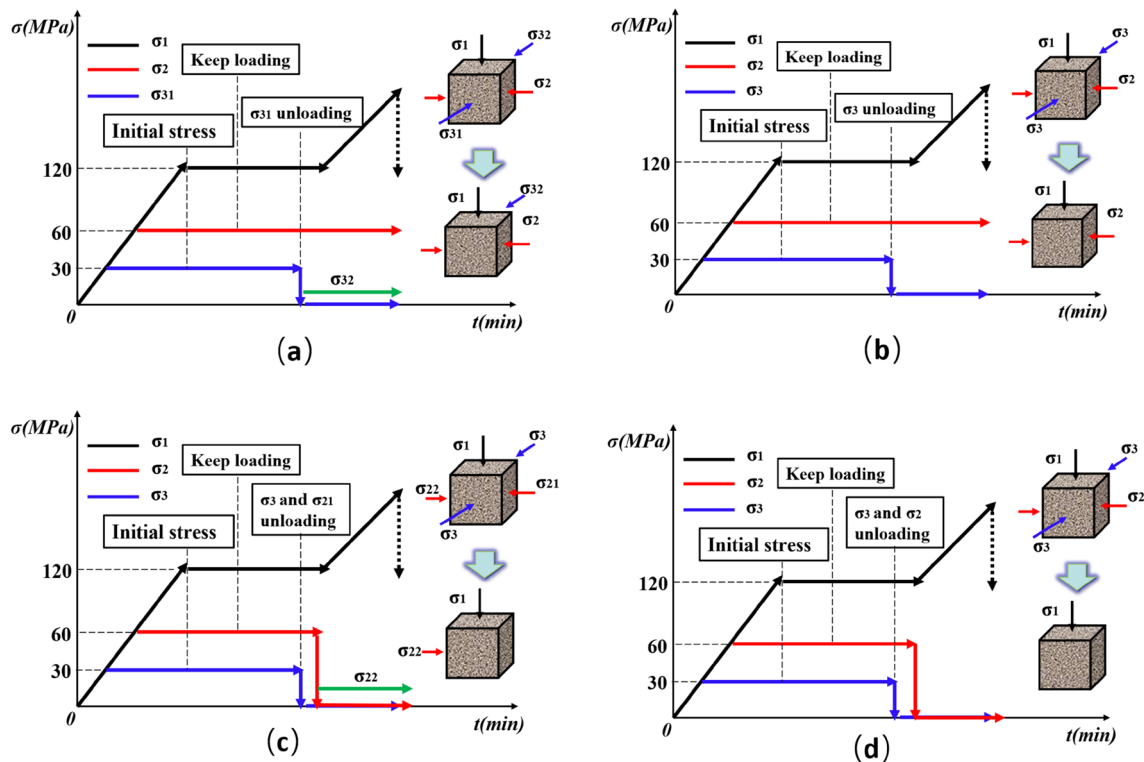


**Fig. 2** True triaxial stress loading path of multi-facet unloading rockburst experiment. **a** Single-side fast unloading, **b** double-side fast unloading, **c** three-side fast unloading, and **d** four-side fast unloading



respectively. The experiment adopts stress control loading, and the loading speed is 2kN/s.

## 2.2 Experimental Sample

To control other variables that affect the experimental results in this experiment, fine-grained red sandstone with relatively high homogeneity was used as the experimental sample, as shown in Fig. 3. The sandstone is selected from Changsha, Hunan, China. The sandstone size is 150 mm cube, and the uniaxial compressive strength is 117.28 MPa. SEM scanned the sandstone, and Fig. 4 shows the 100-fold and 200-fold SEM images of the sandstone sample. The microscopic scanning results show that the cross-section of the sample is composed of coarse-grained crystalline substances, and the cementation between the particles is good, with prominent weak surfaces and voids. SEM observation shows that sandstone is a kind of heterogeneous porous material. Due to the existence of microcracks and original cracks, when the sample is initially loaded, many AE signals will appear due to the compaction of the original cracks. Tables 1 and 2, respectively, list the relative content of the whole rock and the clay mineral composition of the sandstone used in the experiment. Its main minerals are plagioclase, quartz, clay minerals, and a small amount of potassium feldspar, calcite, hematite, and laumontite. Clay minerals are mainly composed of green montmorillonite and illite. It can be seen from the table that the low clay mineral content of sandstone may lead to strong rockburst (He et al. 2020).

## 2.3 True Triaxial Rockburst Experimental System

The new-generation rockburst experimental system was independently developed by the State Key Laboratory of Deep Geotechnical Mechanics and Underground

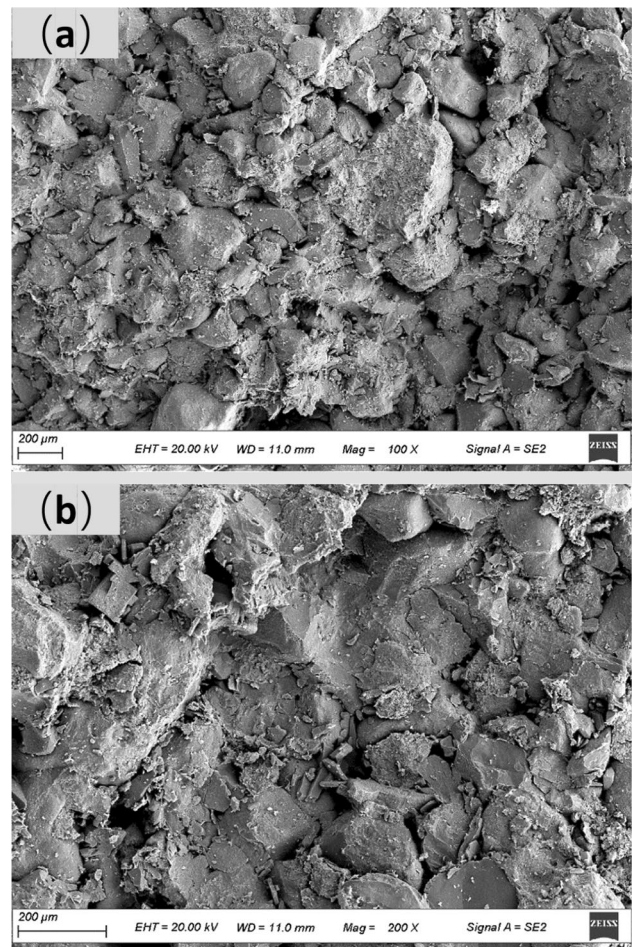


**Fig. 4** Sandstone scanning electron microscope (SEM) pictures. **a** Amplified 100 times, and **b** amplified 200 times

Engineering (Beijing) (He et al. 2021a), as shown in (Fig. 5a, b). The maximum axial loading force of the experimental

**Fig. 3** Experimental samples.

**a** Overview of sandstone specimens, and **b** sandstone specimen

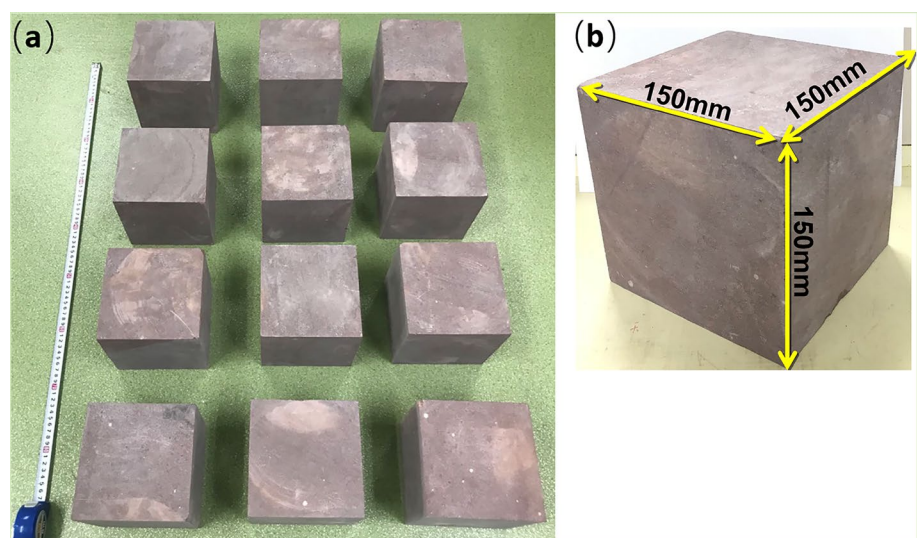


**Table 1** Relative content of mineral components for sandstone

Mineral content (%)						
Quartz	Potash feldspar	Plagioclase	Calcite	Hematite	Laumontite	Clay mineral
16.0	4.2	68.6	2.8	1.3	2.1	5.0

**Table 2** Relative content of clay mineral components for sandstone

Relative content of clay minerals (%)						Mixed layer ratio (%S)	
S	I/S	It	Kao	C	C/S	I/S	C/S
/	/	16	/	/	84	/	50

S smectites, I/S Imon mixed layer, It illite, K kaolinite, C chlorite, C/S green smectite layer

system is 5000 kN, and the maximum horizontal loading force is 2000 kN. The experimental system is equipped with both an AE system and a high-speed camera system to monitor the damage evolution process of internal cracks and the rockburst ejection process during rock loading. The high-speed camera system includes two AcuteEye high-speed cameras (Fig. 5c–e). Each camera can store up to 40 min at 1000 frames/s, with a resolution of  $1024 \times 1024$ . The two cameras are connected to memory through a synchronization controller, which can achieve high-precision synchronous shooting. The AE monitoring equipment used in this experiment (Fig. 5f, g) is shown as the Micro-II acoustic emission monitoring system of PAC Company. Its built-in processor can analyze the sampled signal in real-time, the maximum signal amplitude is 100 dB, and the maximum sampling rate that can be achieved is 40 Msps. The amplifier uses a “2/4/6” type signal amplifier with three amplification levels of 20, 40, and 60 dB, in this experiment, 40 dB is selected. The probe adopts a Nano-30 type sensor (Fig. 5h) whose frequency response range is 100–500 kHz. All probes are placed outside the pressing plate. Vaseline is applied between the ceramic sheet and the pressing plate on the surface of the probe to ensure a close fit. The probe is fixed to the surface of the pressing plate through a resin shell with a magnet. In addition, a reaction spring is placed in the resin shell to ensure close contact.

### 3 Results and Discussions

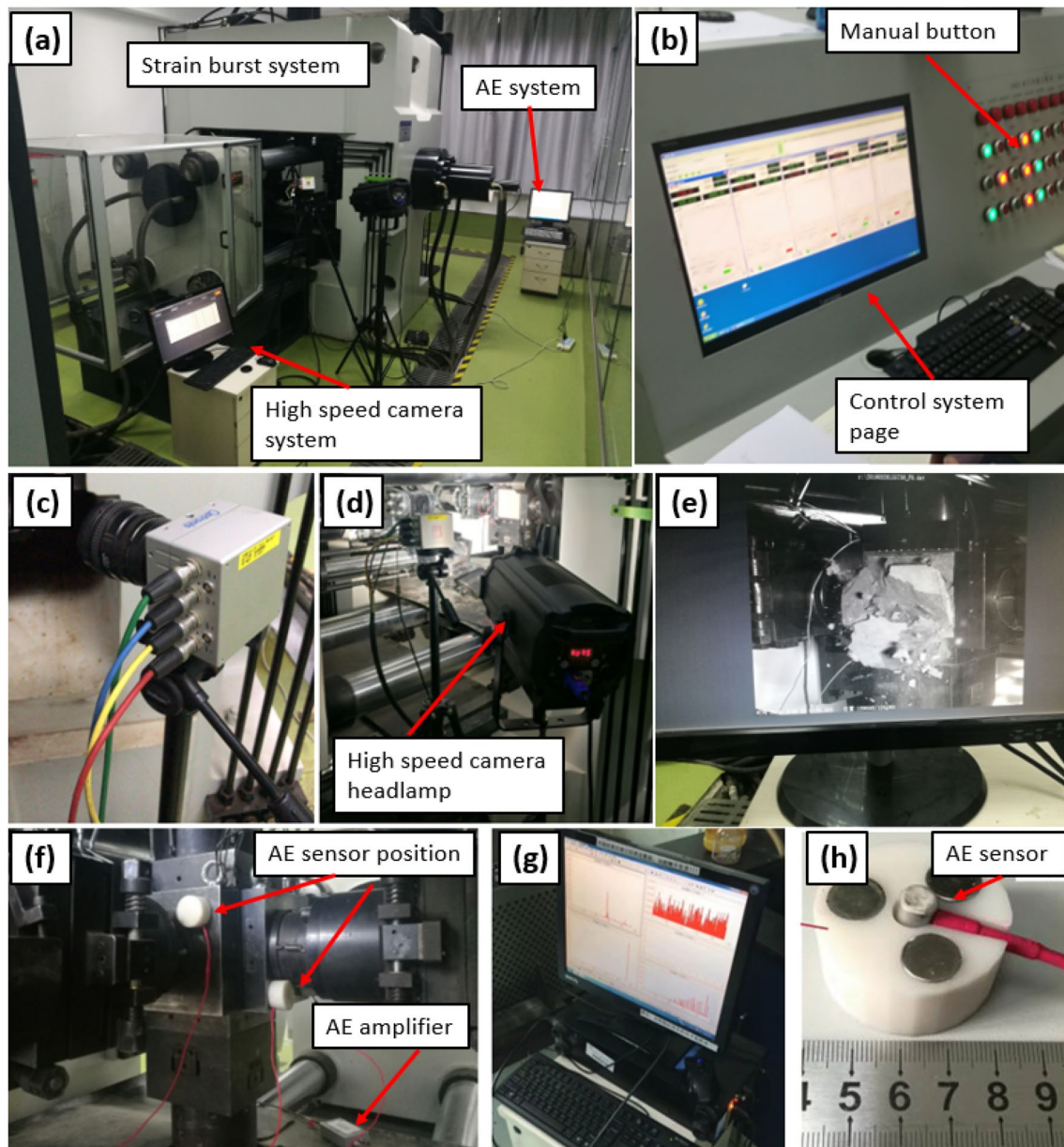
#### 3.1 Analysis of Stress–Strain

Figure 6 is a typical multi-side unloading rockburst stress–strain curve. As the figure shows, the axial stress–strain curve of sandstone can be divided into five stages. Because the four-side unloading rockburst axial stress–strain curve has no yield stage, it is only divided into four stages. As the figure shows, the yield stage of the axial stress–strain curve of the multi-side unloading rockburst of

sandstone is very short, showing prominent brittle characteristics. After the true triaxial stress is loaded to the set initial in-situ stress state, the fast unloading of the horizontal stress is carried out. As the figure shows, there will be an unloading platform. Note: during the fast unloading of horizontal stress, the axial stress remains unchanged. This is because the rapid unloading of sandstone in the horizontal direction under true triaxial high pressure will lead to the expansion of sandstone along the unloading direction. According to the Poisson effect of the rock, the rock will become longer in the horizontal direction and will inevitably become shorter in the axial direction (Gercek 2007). Therefore, the expansion of unloading rock will lead to a sudden increase in axial strain, resulting in a rapid unloading platform. This experiment adopts stress-controlled loading. When the sample shortens in the axial direction, the cylinder needs a more significant displacement to compensate for keeping the stress unchanged, so an unloading platform is created on the stress–strain curve. As the figure shows, the width of the unloading platform increases gradually from the single-side unloading to the four-side unloading axial stress–strain curve, which also shows that with the increase of the NUS, the expansion phenomenon of the sandstone in the unloading direction is more prominent. When the axial stress is loaded to the ultimate stress, the rockburst occurs, the sandstone loses its bearing capacity, and the stress–strain curve after the peak rapidly drops to the minimum value. Through linear fitting of the post-peak curve, it is found that the confining pressure constraint decreases gradually with the increase of the NUS, and the slope of the post-peak stress–strain curve decreases gradually after the rockburst. This is because it is easier for the rock to lose its bearing capacity after the peak when the confining pressure constraint decreases. Table 3 lists the stress and strain parameters of rockburst with multi-side unloading. The drop time of the peak stress in the table refers to the time required for the axial stress to drop from the peak stress to the minimum value after the burst.

It can be seen from Fig. 7a that the axial peak stress of the rockburst decreases gradually with the increase of the





**Fig. 5** Laboratory set-up for multi-side fast unloading rockburst experiment. **a** True triaxial rockburst experiment system, **b** system console, **c** high-speed camera, **d** high-speed camera headlamp, **e**

high-speed camera system record page, **f** AE sensor position, **g** AE system, and **h** AE sensor

NUS, which is caused by the gradual decrease of confining pressure of the rockburst with the increase of the NUS, which is similar to the lower peak strength of rock with the smaller confining pressure in conventional triaxial compression tests (Yang et al. 2020; Yu et al. 2021). It can be seen from Fig. 7b that the axial peak strain of the rockburst gradually decreases with the increase of the NUS, indicating that the peak strain corresponding to the axial peak stress also gradually decreases with the decrease of the confining pressure after the unloading is completed. It can be seen from Fig. 7c that the increment of the axial strain of the rockburst

at the rapid unloading point increases with the increase of the NUS. Figure 7d shows the time taken for the axial peak stress to drop to the minimum value at the bursting point. As the figure shows, with the increase in the NUS, the peak stress decline time is shorter. Hence, the sandstone loses its bearing capacity faster and faster after the burst occurs. The elastic strain energy accumulated in the sandstone is released faster and faster.

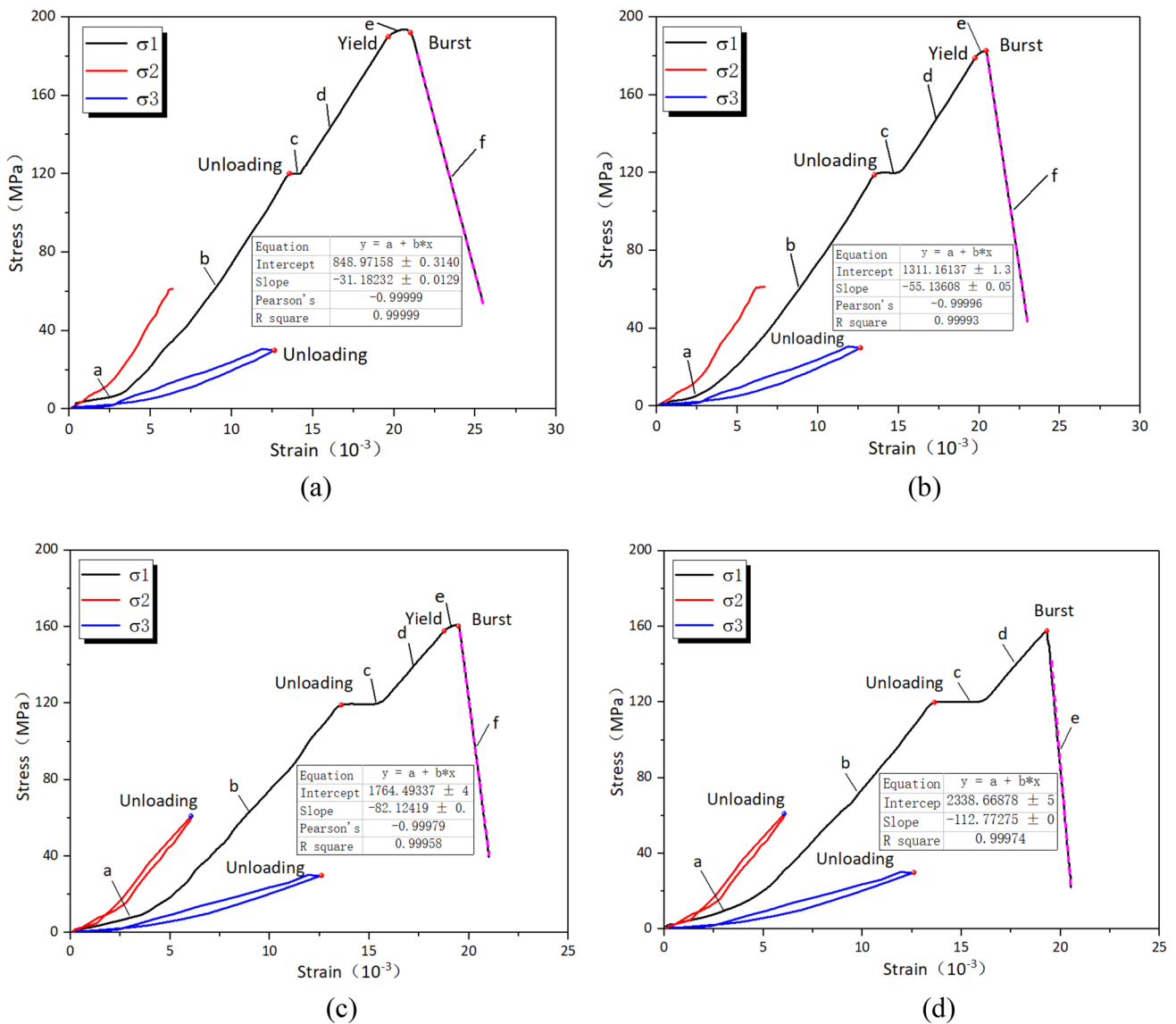


**Fig. 6** Stress–strain curve of multi-side unloading rockburst. **a** Single-side fast unloading, **b** double-side fast unloading, **c** three-side fast unloading, and **d** four-side fast unloading

### 3.2 Analysis of Energy Evolution

Many scholars agree that analyzing rock's damage and failure process under compression from the standpoint of energy is essential. The deformation and failure of rock is essentially a non-equilibrium thermodynamic process that involves energy input, energy accumulation, energy dissipation, and energy release during failure (Zhou et al. 2020; Zhao et al. 2020). The external load is input into the rock in the form of mechanical energy as the deformation degree increases due to the action of the external load. The majority of the energy input by the external load into the loaded rock is converted into reversible elastic energy and stored in the rock's interior during the elastic deformation stage. As the

external load increases, microcracks from within the rock, and the pores gradually expand. This portion of the energy is defined as dissipated energy, and it is primarily used to expand cracks, reducing the rock's ability to resist damage and limiting energy storage (Gong et al. 2021). When the accumulated elastic energy exceeds the energy storage pole, the elastic energy stored within the rock is released, resulting in the rock's destruction. Assuming that there is no heat exchange with the outside world during the test, the work done by the external force for a closed system is the total energy  $U$  absorbed by the sandstone specimen. The total energy  $U$  consists of two parts, one part is the elastic strain energy  $U^e$  stored per unit volume, and the other part is the

**Table 3** Stress–strain parameters of multi-face rapid unloading rockburst

Specimen	Unloading mode	Maximum principal stress			Axial strain at failure point ( $10^{-3}$ )	Strain increment, $\Delta\epsilon$	Peak stress drop time (s)
		$\sigma_1$ (MPa)	$\sigma_2$ (MPa)	$\sigma_3$ (MPa)			
SF#1	Single-side	194.32	60.42	3.56	20.89	0.76	1.15
SF#2		192.58	60.42	3.57	20.64	0.84	1.13
SF#3		195.26	60.43	6.54	21.12	0.81	1.17
DF#1	Double-side	183.37	60.43	0	20.45	1.32	0.98
DF#2		191.85	60.42	0	20.21	1.23	0.96
DF#3		185.42	60.42	0	20.15	1.25	0.98
TF#1	Three-side	161.36	0	3.57	19.50	1.78	0.74
TF#2		163.20	0	4.23	19.53	1.67	0.74
TF#3		165.06	0	3.15	20.07	1.84	0.72
FF#1	Four-side	157.23	0	0	19.27	2.53	0.66
FF#2		159.42	0	0	20.15	2.54	0.72
FF#3		158.37	0	0	19.54	2.61	0.62

dissipation energy  $U^d$  used for the evolution of cracks in the rock.

$$U = U^e + U^d \tag{1}$$

$$U = \int_0^{\epsilon_1} \sigma_1 d\epsilon_1 + \int_0^{\epsilon_2} \sigma_2 d\epsilon_2 + \int_0^{\epsilon_3} \sigma_3 d\epsilon_3 \tag{2}$$

$$U^e = \frac{1}{2}\sigma_1\epsilon_1^e + \frac{1}{2}\sigma_2\epsilon_2^e + \frac{1}{2}\sigma_3\epsilon_3^e \tag{3}$$

From Hooke’s theorem, Eq. (3) can be rewritten as:

$$U^e = \frac{1}{2E_0} [\sigma_1^2 + \sigma_2^2 + \sigma_3^2 - 2\nu(\sigma_1\sigma_2 + \sigma_2\sigma_3 + \sigma_1\sigma_3)] \tag{4}$$

where  $E_0$  is the initial elastic modulus and  $\nu$  is Poisson's ratio. Since the loading to the initial stress value belongs to true triaxial 3D loading, the four groups of experiments are under the same loading path, and the energy input is the same. After the unloading is completed, the energy input is mainly provided by the stress in the axial direction. This study only calculates the energy evolution in the axial direction to only reflect the influence of the NUS on the rockburst. The research on the energy of the true triaxial rockburst experiment carried out by their scholars also only uses the axial strain to calculate (Chen et al. 2019; He et al. 2021b). Therefore, the calculation formula of elastic strain energy can be simplified as follows:

$$U^e = \frac{1}{2E_0}\sigma_1^2 \tag{5}$$

Based on the concept of a definite integral, the calculation formula for the total energy is:

$$U = \sum_i^n \frac{1}{2}(\sigma_1^i + \sigma_1^{i+1})(\epsilon_1^{i+1} - \epsilon_1^i) \tag{6}$$

where  $\sigma_1^i$  and  $\epsilon_1^i$  are the stress and strain values of each point in the stress–strain curve, respectively. Therefore, the dissipated energy  $U^d$  of the rock during the test can be obtained as follows:

$$U^d = U - U^e \tag{7}$$

Parameters  $U$ ,  $U^e$ , and  $U^d$  during the entire process of deformation and failure of the rock sample were calculated using the energy calculation principle. The variation relationship between the typical multi-side unloading rockburst energy curve and the axial stress–strain curve is shown in Fig. 8. It can be seen from the figure that the energy evolution of the rockburst with different NUS has the same change trend. According to the local magnification of single-side unloading rockburst in Fig. 8a in the initial compaction stage, it can be seen that in the initial compaction stage, the growth rate of dissipated energy is greater than that of elastic strain energy due to the closure and friction of micro-cracks in sandstone samples. With the increase of pressure, it enters the elastic deformation stage. Due to true triaxial confining pressure, almost all the total energy input into the sandstone system is converted into elastic strain energy. With the increase of deformation, the accumulation rate of elastic strain energy begins to increase, and the growth rate of dissipated energy decreases. When the elastic strain energy curve intersects with the dissipated energy curve, the growth rate of elastic strain energy begins to be greater than the dissipated energy. It is consistent with the growth rate of the total input energy of the system. It can be seen from the figure that the dissipated energy has a sudden increase at the rapid unloading point, which is due to the damage in the



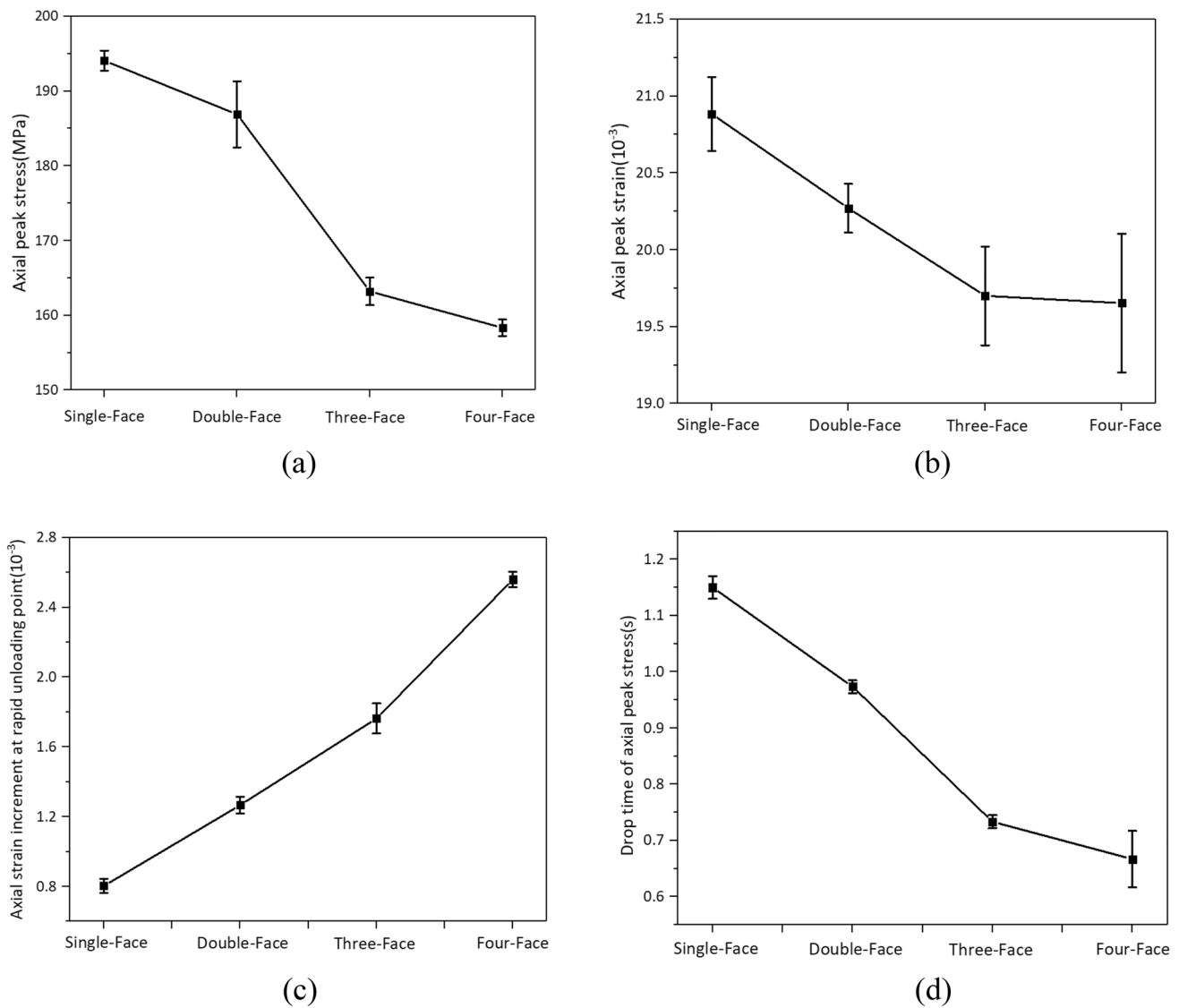


**Fig. 7** Variation curve of stress–strain parameters with the NUS. **a** Axial peak stress, **b** axial peak strain, **c** axial strain increment at fast unloading point, and **d** drop time of axial peak stress

rock caused by rapid unloading along the unloading direction, so the dissipated energy has a sudden increase. After rapid unloading, the axial stress continues to increase. At this time, the rock is still in the stage of linear elastic deformation. All the energy input by the system is transformed into elastic strain energy. With the increase of axial stress, the burst occurs when the elastic strain energy stored in the rock sample reaches the energy storage limit.

It can be seen from Table 4 that with the increase of the NUS, the total energy input by the axial stress of rockburst at the peak point, the elastic strain energy, and the total energy input by the system gradually decrease, while the dissipated energy gradually increases. This is because with the increase of the NUS, the confining pressure constraint of sandstone decreases, the stress and strain

during rockburst gradually decrease, and the total energy and elastic strain energy input by the system in sandstone decreases. With the confining pressure constraint of sandstone decreases, and the sandstone is more prone to damage in the loading process after rapid unloading, so the dissipated energy increases gradually. It can be seen from the table that the difference between the total energy input by the system at the peak point and the total energy input by the system after the burst gradually decreases with the increase of the NUS. It shows that after the rock reaches the peak point, its failure only needs little external force to do work, and the sudden release of the strain energy stored in the rock sample can make its fracture continue to develop. Therefore, it shows stronger brittleness with the increase in the NUS. It can be seen from the table

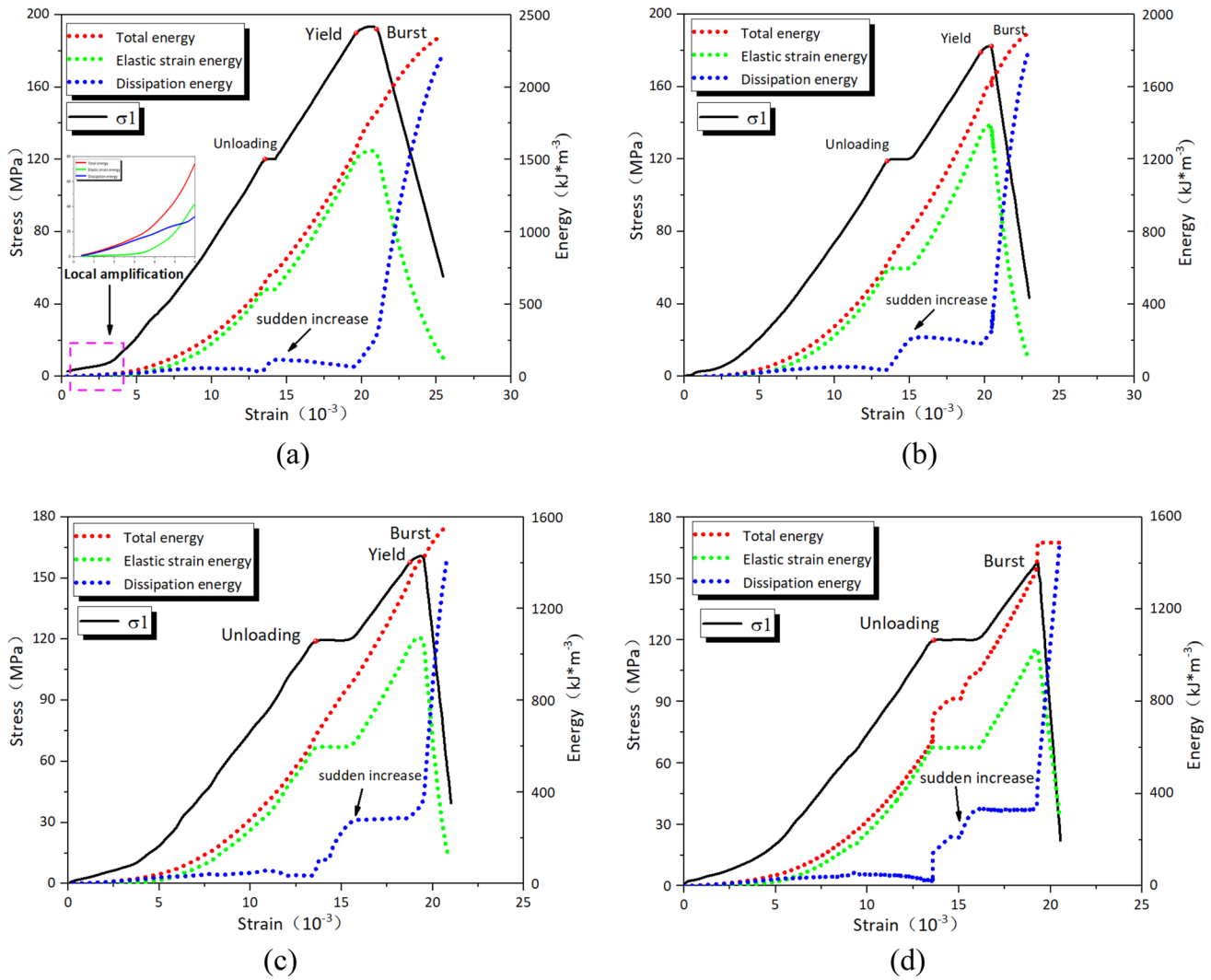


**Fig. 8** Multi-side unloading rockburst energy evolution, **a** single-side fast unloading, **b** double-side fast unloading, **c** three-side fast unloading, and **d** four-side fast unloading

**Table 4** Energy parameters of multi-face rapid unloading rockburst

Specimen	Unloading mode	Total energy at peak point	Peak point elastic strain energy	Total input energy	Peak point dissipated energy	Dissipative energy increment at unloading point	Elastic strain energy release rate
SF#1	Single-side	1758.3	1530.4	2403	227.9	87.7	1359.5
SF#2		1746.9	1532.1	2579.4	214.8	85.3	1355.8
SF#3		1709.3	1543.2	2569.1	166.1	85.8	1318.9
DF#1	Double-side	1645.2	1387.7	1919	257.5	186.8	1416
DF#2		1628.7	1380.8	1925.1	247.9	154.3	1438.3
DF#3		1634.9	1374.5	1922.4	260.4	176.3	1402.6
TF#1	Three-side	1452.8	1073.2	1575.5	379.6	248.6	1450.3
TF#2		1456.9	1075.6	1589.6	381.3	236.1	1452.7
TF#3		1466.5	1084.9	1593	381.6	273.5	1506.8
FF#1	Four-side	1481.8	1021.8	1489.5	460.0	309.2	1548.1
FF#2		1504.3	1089.4	1507.3	414.9	287	1512.5
FF#3		1485.5	1023.1	1485.7	462.4	303.7	1650.3

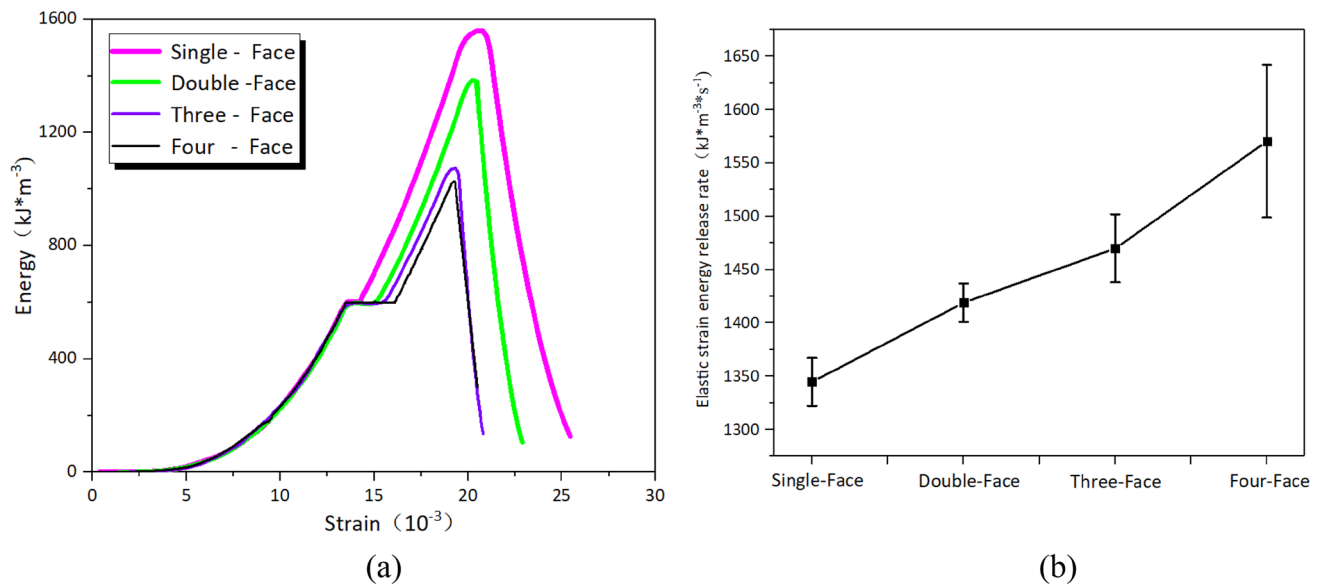


**Fig. 9** Release rate of elastic strain energy of multi-side unloading rockburst, **a** comparison of elastic strain energy of multi-faceted unloading rockburst, and **b** release rate of elastic strain energy during rockburst varies with the NUS

that with the increase of the NUS, the increment of dissipated energy of the rockburst at the fast unloading point gradually increases, indicating that the more NUS under high pressure, the greater the unloading damage to sandstone. Figure 9a shows the comparison diagram of elastic strain energy stored in rockburst with the different NUS. It can be seen from the figure that with the increase in the NUS, the ability to store elastic strain gradually decreases due to the decrease of confining pressure constraint. It can be seen from the figure that after the elastic energy is stored to the limit, the slope of elastic strain energy drop increases with the increase of the NUS, indicating that the release rate of elastic strain energy increases. The elastic strain energy release rate is defined by dividing the elastic strain energy stored at the peak point by the drop time of the peak stress. Figure 9b shows the variation trend of the release rate of elastic strain energy with the increase in the NUS. It can be seen from the figure that with the increase in the NUS, the release rate of elastic strain energy at the peak point of axial stress increases during the rockburst, so the burst is also more intense. This shows that the intensity of a rockburst depends on the release rate of elastic strain energy at the time of the burst rather than the amount of energy stored in the rock before failure.

The elastic energy consumption ratio is defined as the ratio of dissipated energy to elastic strain energy, demonstrating the proportional relationship between energy storage and energy consumption throughout rock sample deformation and failure (Wang et al. 2019).

$$K = \frac{U^d}{U^e} \quad (8)$$

The elastic energy consumption ratio  $K$  and the stress–strain curve during the multi-side fast unloading rockburst loading process are plotted in Fig. 10. For the multi-side unloaded rockburst, the energy dissipation occurs due to the closure of microcracks in the initial compaction stage. The elastic energy consumption ratio increases sharply because the growth rate of the initial dissipated energy is greater than that of the elastic strain energy. After reaching the maximum value, as the microcracks gradually closed, the elastic strain energy accumulation rate increased. The dissipated energy growth rate decreased, so the elastic energy consumption ratio began to decrease gradually with the strain and finally became stable. After loading to the initial in-situ stress state, the rapid unloading of the horizontal loading surface is carried out. Since the fast unloading causes a sudden increase in the dissipation energy while the elastic strain energy remains unchanged, the elastic energy consumption ratio at the fast unloading point has a sudden increase, which also means that the rapid unloading causes unloading damage to the sandstone. Subsequently, the elastic energy consumption ratio suddenly changes at the peak stress, indicating that the rock sample will suffer from rockburst failure, consistent with the conclusion reported in (Wang et al. 2019). Figure 11a lists the sudden value of the elastic energy consumption ratio  $K$  at the point of rapid unloading. The figure shows that with the increase of the NUS in the horizontal direction, the sudden value of the  $K$  value

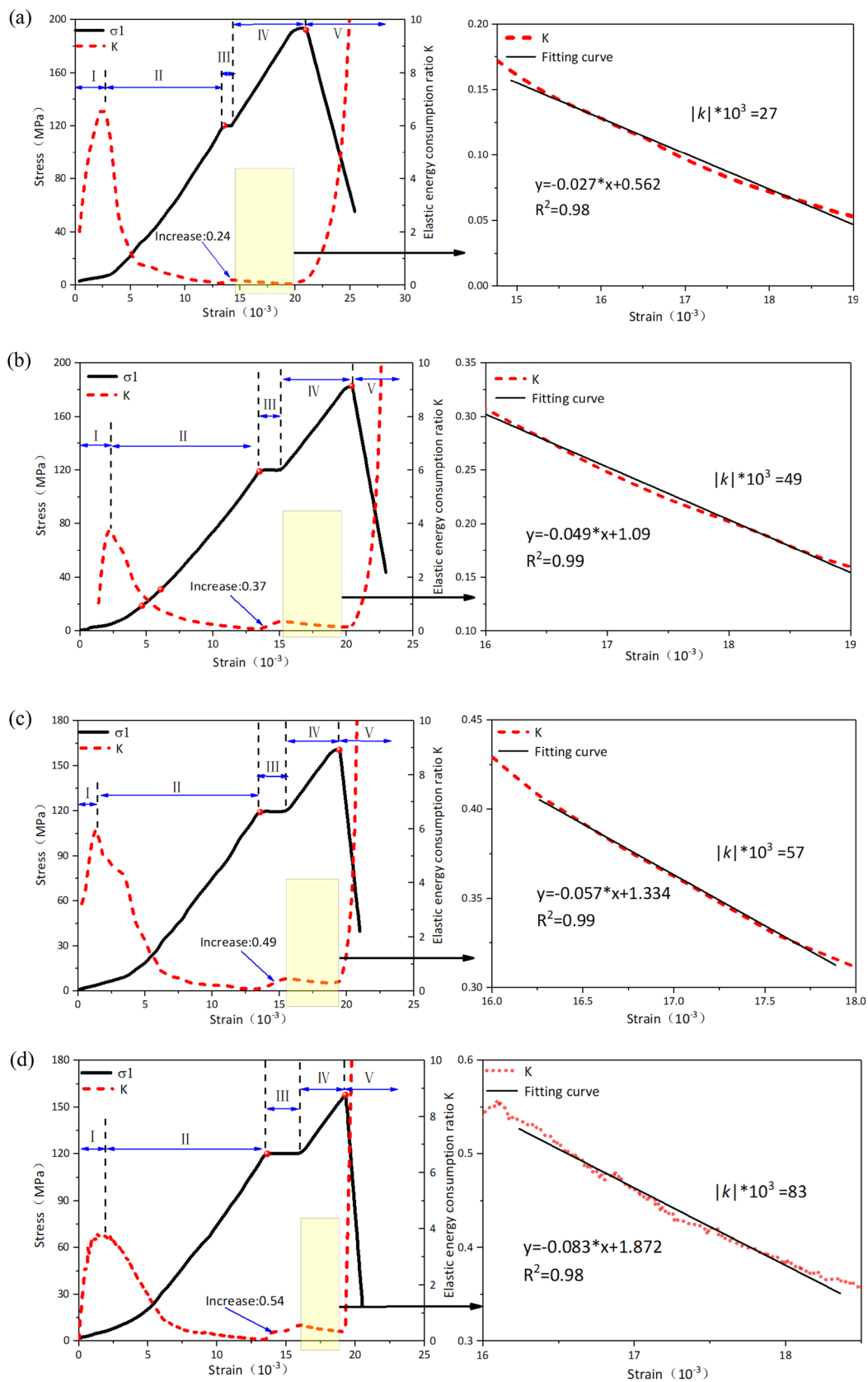


**Fig. 10** Energy dissipation ratio of multi-side fast unloading rockburst, **a** single-side fast unloading, **b** double-side fast unloading, **c** three-side fast unloading, and **d** four-side fast unloading

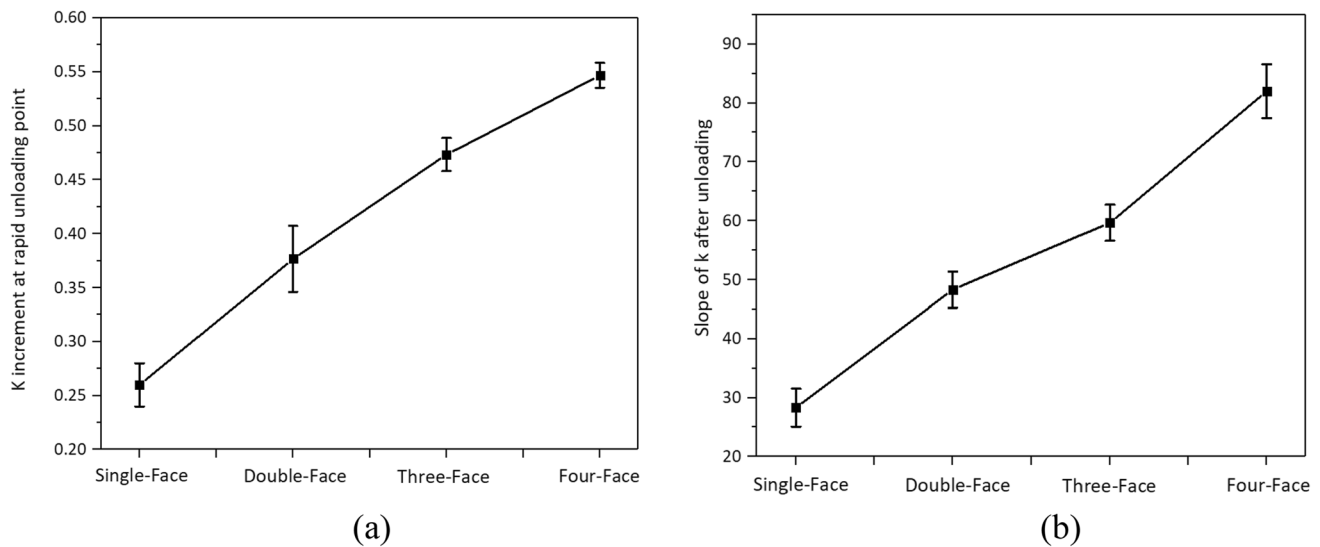


**Fig. 11** **a**  $K$  increment at fast unloading point with the NUS, and **b** slope of  $K$  after unloading with the NUS

at the fast unloading point increases gradually, indicating that the unloading damage caused by the fast unloading gradually increases. Figure 11b lists the absolute value of the decreasing slope of the elastic energy consumption ratio from the end of unloading to the peak stress segment. The figure shows that with the increase in the NUS, the dissipative energy gradually increases after the unloading is completed due to the horizontal restraint gradually decreasing, so the slope of the  $K$  value gradually increases.

### 3.3 Analysis of Failure Characteristics

To observe the fragment ejection process during the failure of multi-side fast unloading rockburst. Using high-speed camera technology, the dynamic failure characteristics of the specimens were observed at a frame rate of 1000f/s. Figure 12 shows the failure ejection process of the multi-side fast unloading rockburst, and the numbers below each figure are the times when the corresponding phenomenon occurs. The figure shows that the burst destruction ejection process has the same characteristics. First, there will be cracks on the free surface of the sandstone, and then there will be spalling and ejection of small fragments, and finally, the burst will fully erupt. Due to the anisotropic characteristics of the rock, the ejection failure process of the free surface is not the same. It can be seen from the figure that the rockburst becomes more and more severe with the increase in the NUS, which is caused by the gradual reduction of the horizontal binding force and the increase of the free surface of energy released when the rockburst occurs. With the increase of NUS, although the rock's storage elastic strain energy decreases, the rockburst becomes more and more severe due to the increase of energy release rate. It can be

seen from the figure that the depth and area of the crater gradually increase with the increase of the NUS after the occurrence of a rockburst, which is due to the reduction of confining pressure constraint, and more damaged rock fragments are brought out during the rockburst.

After the rockburst, the ejection fragments on the free surface are collected and screened by the screening instrument. The particle sizes are 10, 5, 2, 1, 0.5, 0.25 and 0.075 mm. Figure 13a shows typical single-side unloading rockburst ejection fragments screening. After screening, weigh the mass of debris in each particle size range. Figure 13b shows the total mass of fragments with different particle sizes in multi-side unloading rockburst. The figure shows that the mass of fragments with particle size greater than 10 mm accounts for more than 75% of the total mass. It can be seen from Fig. 13b, c that the mass of rockburst ejection fragments gradually increases with the increase of the NUS. The thickness of fragments with particle size greater than 10 mm from multi-side unloading rockburst ejection is measured, and the average thickness is calculated. As shown in Fig. 13c, the average thickness of fragments greater than 10 mm gradually increases with the increase in the NUS. The relative thickness of the fragments produced by single-side unloading and double-side unloading rockburst is thinner. This is because when unloading rapidly is equivalent to applying tensile stress to the rock in the unloading direction, causing a large number of tension cracks near the free surface of the sandstone. When a rockburst occurs, the fragments containing many tension cracks near the free surface are ejected. Since the confining pressure constraint of three-side and four-side unloading is very small, the ejected fragments are not only fragmented near the free face but also fragments with internal damage. Hence, the average



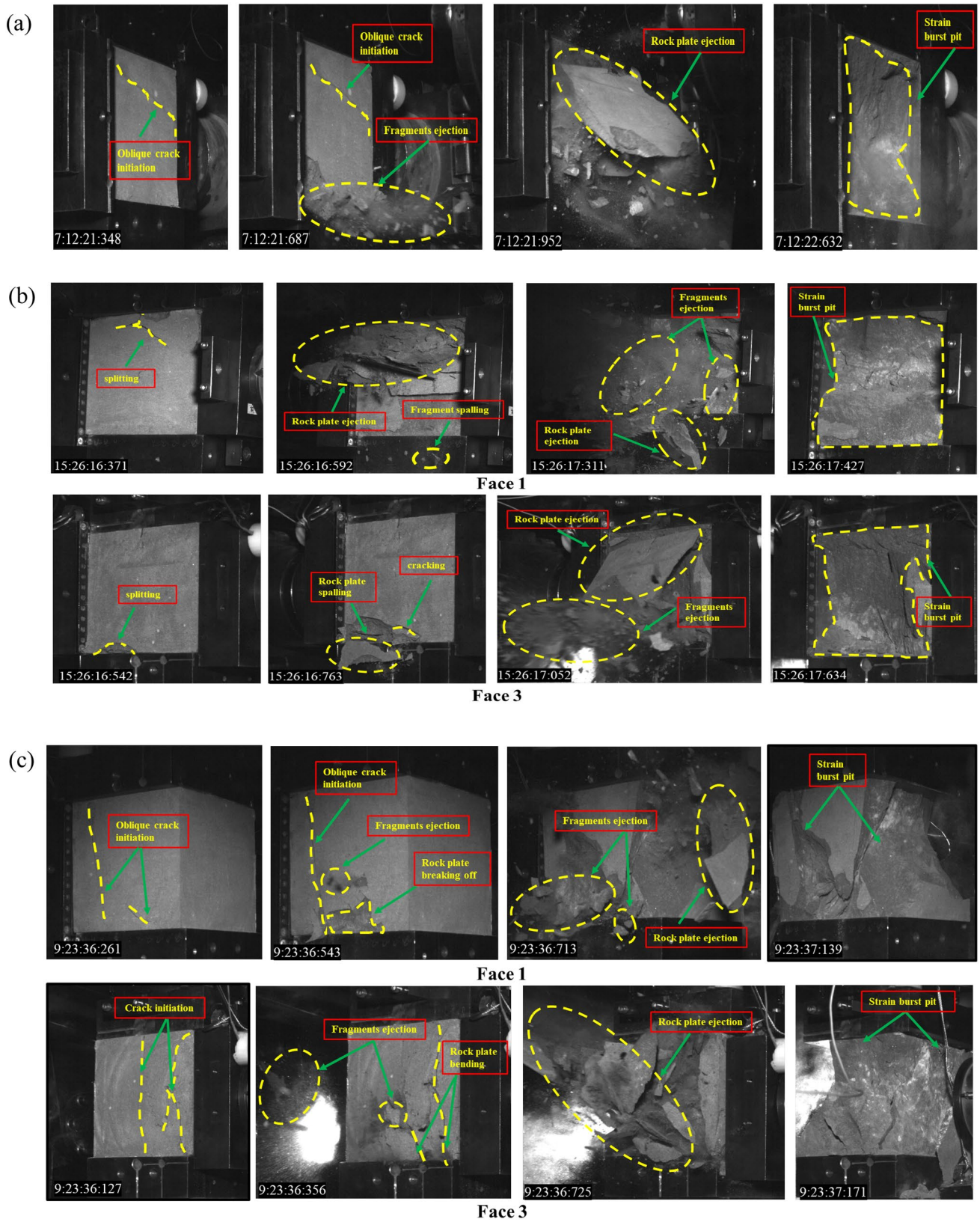


Fig. 12 Failure process of multi-side fast unloading rockburst. **a** Single-side fast unloading, **b** double-side fast unloading, **c** three-side fast unloading, and **d** four-side fast unloading

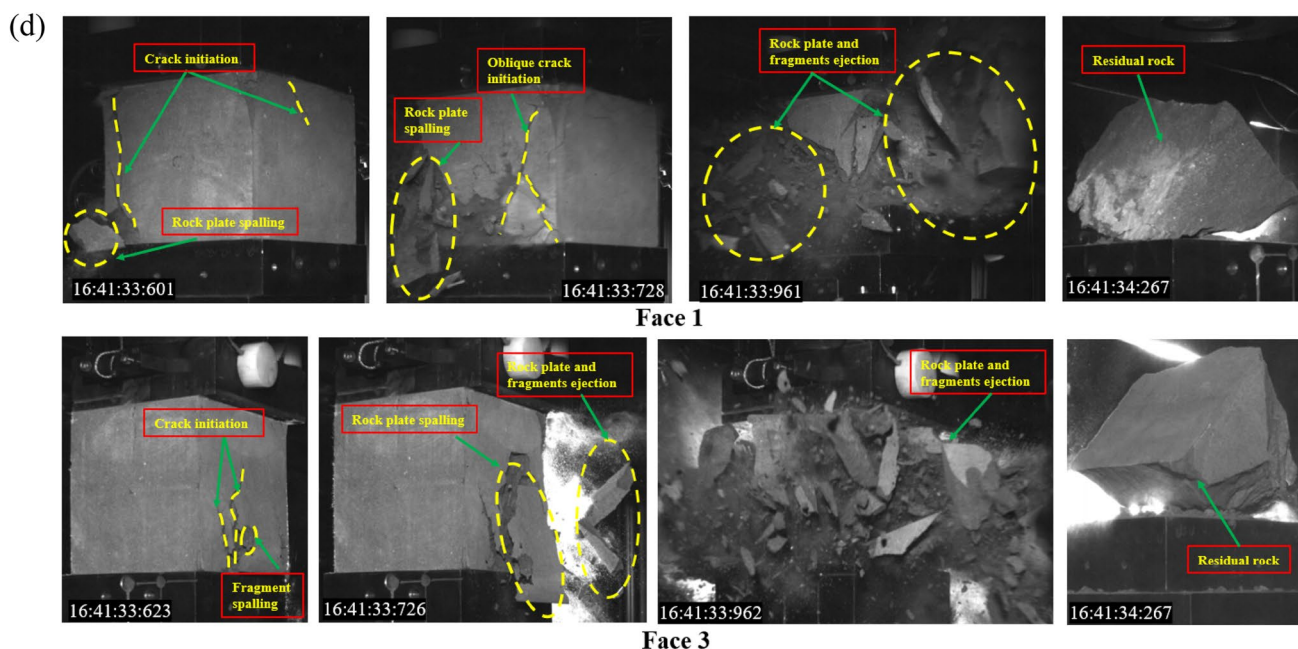


Fig. 12 (continued)

thickness of the ejected fragments of three-side unloading and four-side unloading rockburst is relatively thick.

### 3.4 Analysis of AE

#### 3.4.1 AE Hits Characteristics

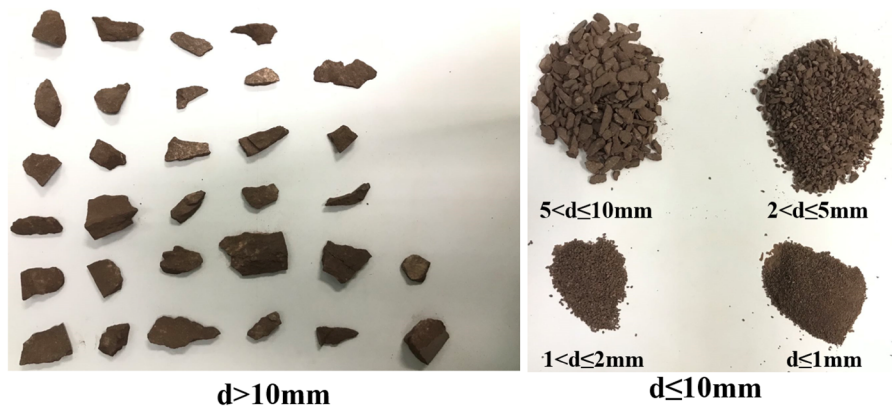
The occurrence of microfractures in the rock mass is accompanied by AE signals' rapid release and propagation. The AE signal contains the spatial information of the complex structure distribution inside the material and carries much essential information in the process of rock fracture evolution (He et al. 2010; Ren et al. 2020). Figure 14 shows the time stress AE hits and cumulative hits evolution diagram of multi-faceted unloading rockburst. It can be seen from the figure that the evolution trend of AE hits of multi-unloading rockburst is the same, and it can be divided into five stages according to the evolution trend. In the initial loading stage, the axial stress is minor, and the primary pores and microcracks in the sandstone are compressed and closed. A small number of AE hits are generated at this time, and the cumulative hits curve rises slightly from zero. The AE hits almost disappears in the elastic stage, and the cumulative hits curve is relatively straight. This is because the rock enters the linear elastic deformation process after the internal primary crack is closed, and the rock is almost not damaged in this stage. With the loss of confining pressure after unloading, more AE hits are generated at this stage with the increase of axial direction, and the cumulative hits curve starts to bend upward. As the axial stress increases to near the peak

stress, the AE hits increases exponentially, and the slope of the cumulative hits curve increases rapidly, reaching the maximum value when a rockburst occurs. The evolution law of AE hits under rockburst loading is consistent with the conclusion of AE research on rock mechanics carried out by many scholars. However, it can be seen from Fig. 14 that the AE hits has a sudden increase at the unloading point, a phenomenon not found in the AE characteristics of rock under conventional loading. This is because the rapid unloading of sandstone on the horizontal loading surface under true triaxial high pressure will produce unloading damage, which will lead to a large number of microcracks in sandstone, leading to the sudden increase of AE signal at the rapid unloading point. Figure 15a shows the cumulative AE hits at the rockburst point changing with the NUS. It can be seen from the figure that the intensity of the rockburst increases with the increase of the NUS, and the cumulative AE hits at the rockburst point gradually increases. It can be seen from Fig. 15b that the sudden increase in the cumulative AE hits at the rapid unloading point of rockburst increases with the increase of the NUS, indicating that the unloading damage gradually increases with the increase of the NUS.

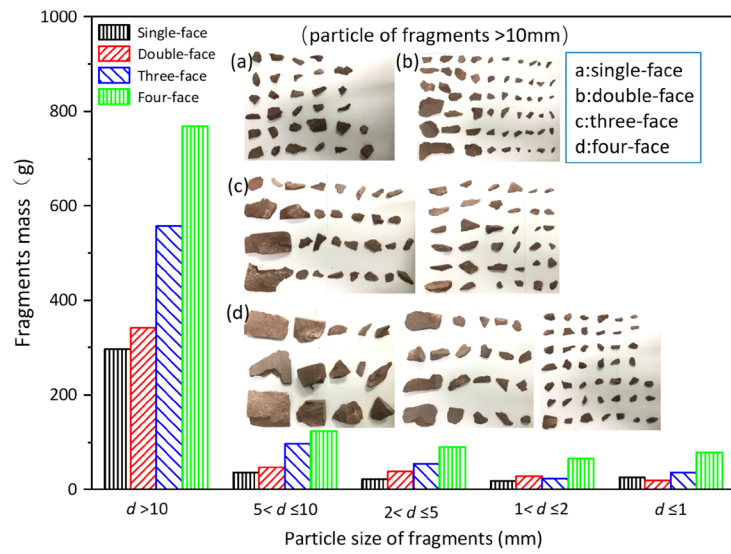
#### 3.4.2 AE Multifractal Feature

Multifractals can describe the inhomogeneity and complexity of things in more detail, and a large number of AE signals generated by rock failure are also nonlinear and discrete (Liu et al. 2013; Lee et al. 2017). Therefore, using the multifractal

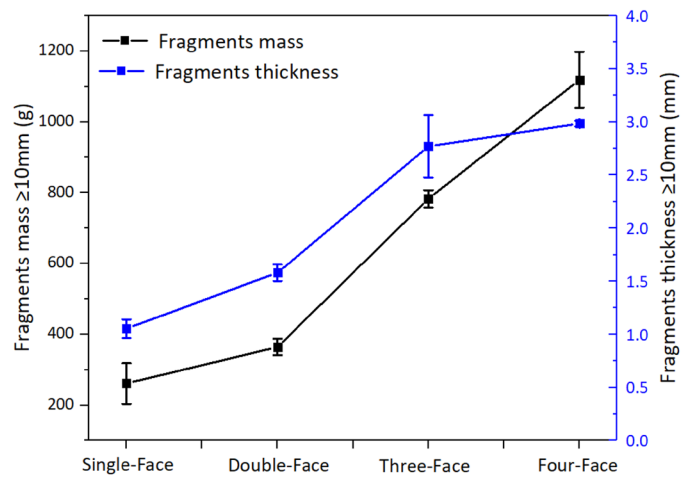
**Fig. 13** Multi-side fast unloading rockburst fragments. **a** Single-side unloading rockburst fragments, **b** distribution of mass percentage of fragments, and **c** the mass and thickness of fragments ( $\geq 10$  mm) vary with the NUS



(a)



(b)



(c)



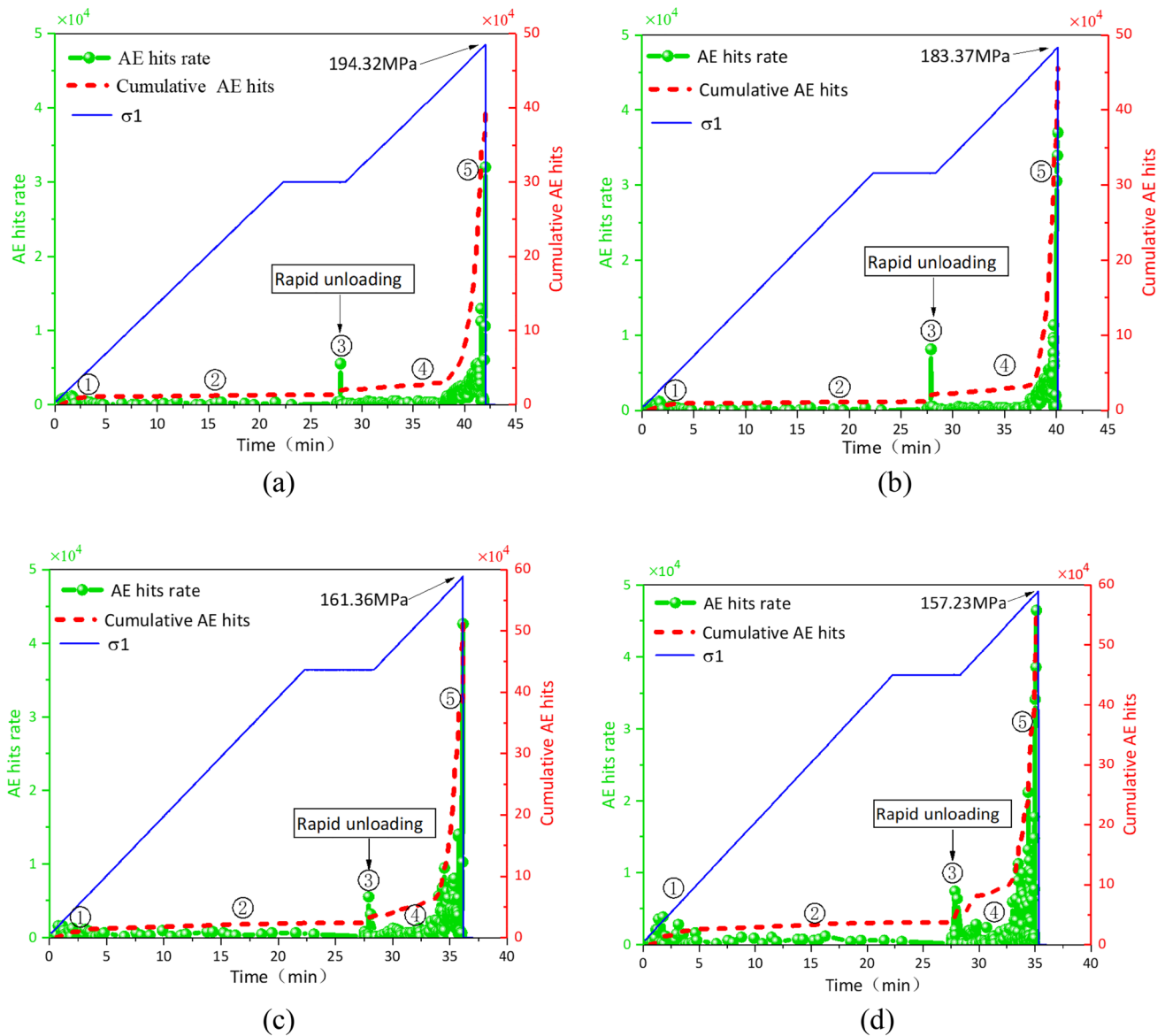


**Fig. 14** AE hits of multi-side fast unloading rockburst. **a** Single-side fast unloading, **b** double-side fast unloading, **c** three-side fast unloading, and **d** four-side fast unloading

method to analyze the AE signal can better reveal the inherent fracture mechanism of the multi-face rapid unloading strain burst. In this paper, the box-counting method is used to calculate the multifractal spectrum of the AE counts time series of the strain burst with different unloading surface numbers during the loading process. Let the time series be  $\{Ti\}$ , the time series can be divided into  $N$  subsets of length  $n$ , and the probability distribution of each subset  $\{Pi(n)\}$  is calculated at the same time. The following formula (Xiong et al. 2016):

$$x_q(n) \equiv \sum p_i(n)^q - n^{\tau(q)} \tag{9}$$

In the formula:  $x_q(n)$  is the function that defines the distribution,  $\tau(q)$  is the quality index,  $-\infty < q < +\infty$ .  $q$  is the weighting factor. The size of the  $q$  value indicates the degree of inhomogeneity of the multifractal. Generally, the  $q$  value is limited to a certain range. In this paper, the value of  $q$  is from  $-20$  to  $20$ . Transform formula (9) to calculate the value of  $\tau(q)$  (Xiong et al. 2016):

$$\tau_q = \lim_{n \rightarrow 0} \frac{\ln T_q(n)}{\ln n} \tag{10}$$

Applying the Legendre transform of Eq. (2) to  $\tau(q)$ - $q$  can obtain (Kong et al. 2016):

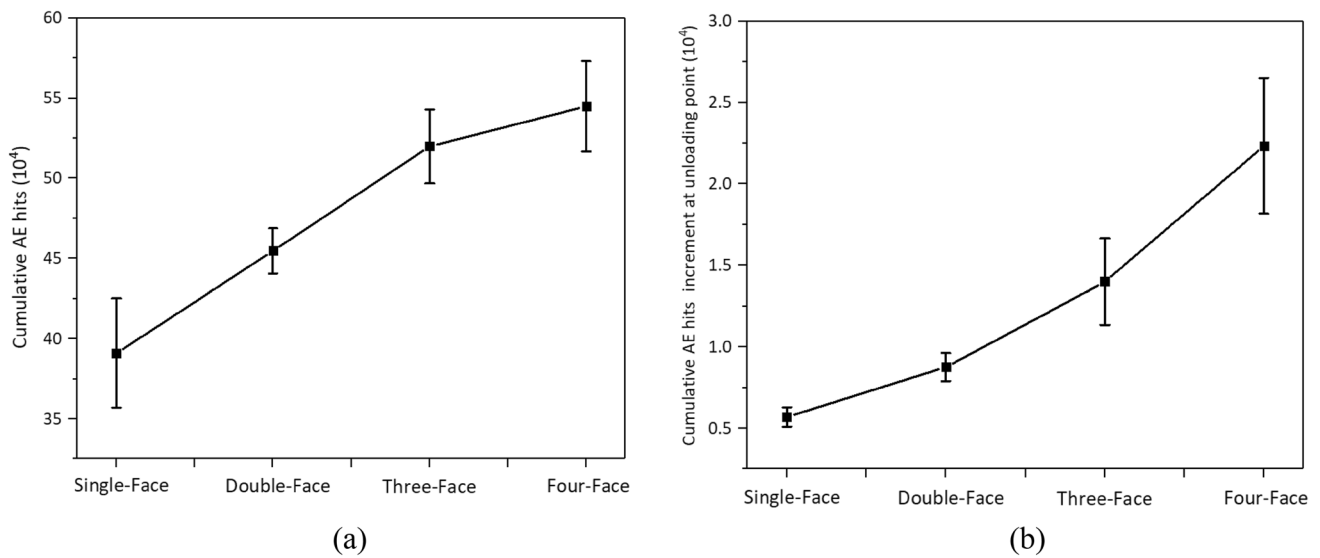


Fig. 15 a Cumulative AE hits at burst point with the NUS, and b cumulative AE hits increment at unloading point with the NUS

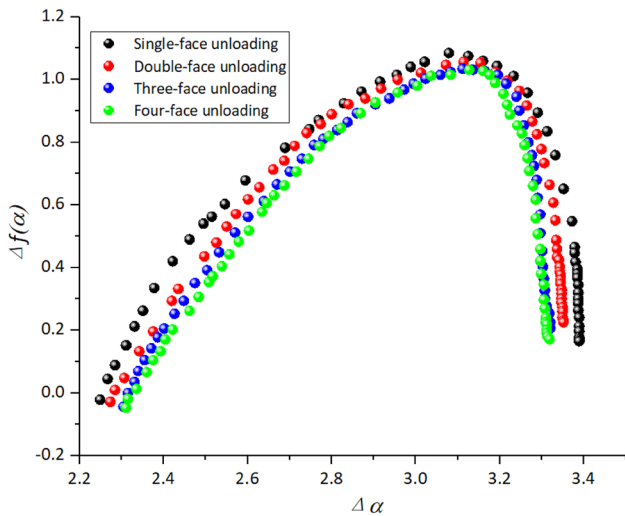


Fig. 16 AE multifractal spectrum of multi-side fast unloading rockburst

$$\alpha = \frac{d(\tau(q))}{dq} = \frac{d}{dq} \left( \lim_{n \rightarrow 0} \frac{\ln T_q(n)}{\ln n} \right) \tag{11}$$

$$f(\alpha) = \alpha q - \tau_q \tag{12}$$

Among them,  $\alpha$  is the singularity index, which mainly reflects the singularity of  $\{Pi(n)\}$ , and shows the inhomogeneous degree of the probability subset.  $f(\alpha)$  is expressed as the fractal dimension of the subset of  $\alpha$ . The  $\alpha - f(\alpha)$  relationship curve is the multifractal spectrum of the calculation sequence, which can reflect the inhomogeneity and randomness of the signal. The larger

the multifractal spectrum width  $\Delta\alpha = \alpha_{max} - \alpha_{min}$ , the more severe the signal distribution fluctuation. And  $\Delta f(\alpha) = f(\alpha_{max}) - f(\alpha_{min})$  represents the frequency relationship of different energy signals. The smaller  $\Delta f(\alpha)$ , the more high-energy signals, and the higher the rock fracture degree (Kong et al. 2017).

Figure 16 shows the multifractal spectrum of the sandstone multi-side unloading rockburst AE. The basic shape of the multifractal spectrum of the sandstone with different unloading faces is the same. All show a trend of  $\Delta f(\alpha)$  increasing first and then decreasing with the increase of  $\Delta\alpha$ , indicating that the evolution of internal cracks in sandstone rockburst with different NUS has a certain similarity. Since the width of the multifractal spectrum is not the same, it shows that there are differences in the microscopic fracture characteristics of the sandstone strain burst evolution process with different NUS.

Figure 17 shows the variation relationship between  $\Delta f(\alpha)$  and  $\Delta\alpha$  with stress-strain curves of typical rockburst with different NUS. It can be seen from the figure that the corresponding multifractal parameters  $\Delta\alpha$  and  $\Delta f(\alpha)$  at different stages of the stress-strain curve show obvious differences. In the initial stage of loading (a), due to the closure of primary fractures in the sandstone,  $\Delta\alpha$  is at a small value, while  $\Delta f(\alpha)$  is at a larger value. During this process, the  $\Delta\alpha$  and  $\Delta f(\alpha)$  of the sandstone rockburst with different NUS fluctuated slightly, and the overall trend was that  $\Delta\alpha$  was upward and  $\Delta f(\alpha)$  was downward, and the multifractal feature was weak. In section (b), both  $\Delta\alpha$  and  $\Delta f(\alpha)$  remain stable as the sandstone enters the linear elastic stage. In section (c), due to the rapid unloading of the stress in the horizontal direction,  $\Delta\alpha$  increases,  $\Delta f(\alpha)$  decreases, and the multifractal characteristics are



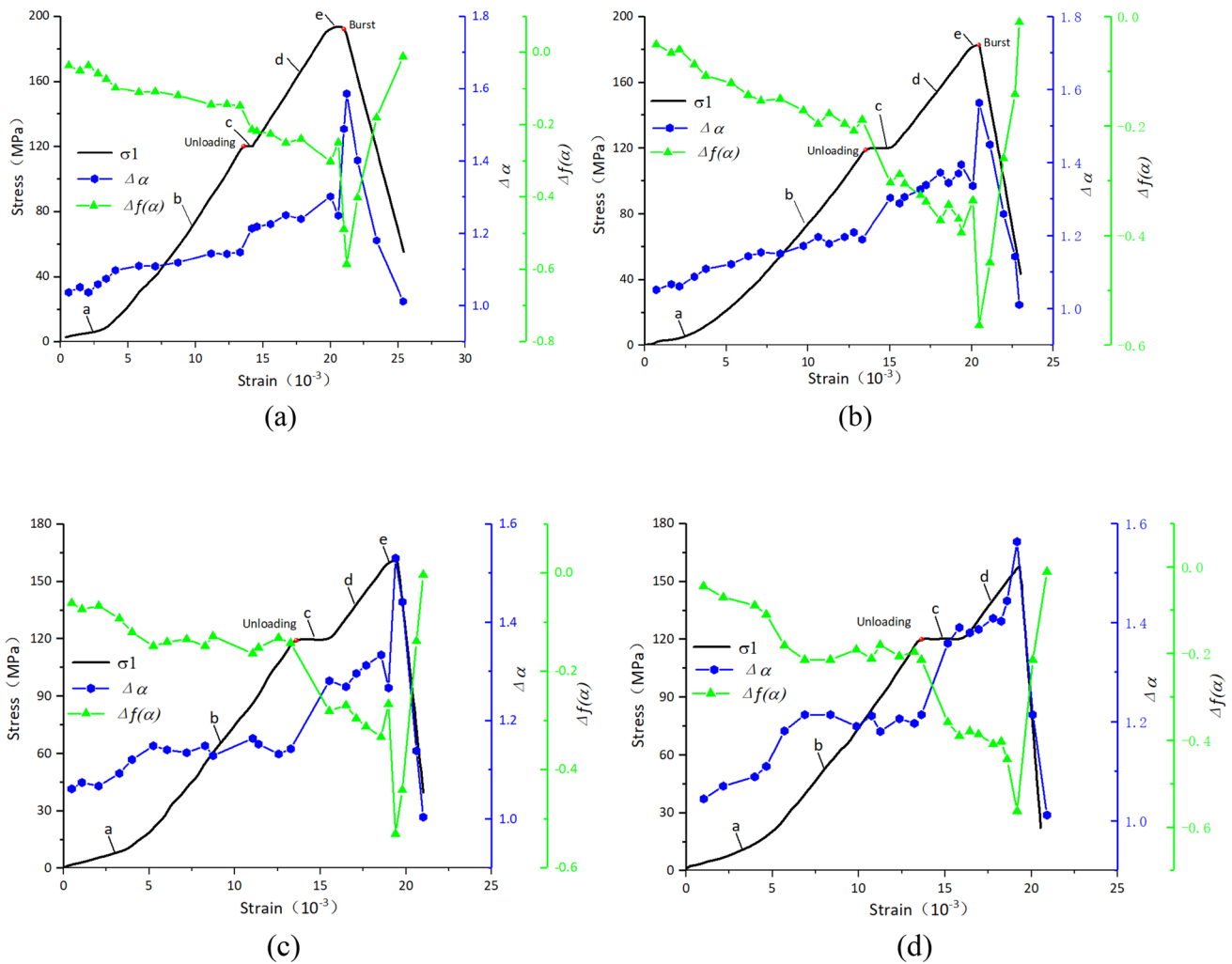


**Fig. 17** The variation curves of multifractal characteristic for multi-side fast unloading rockburst. **a** Single-side fast unloading, **b** double-side fast unloading, **c** three-side fast unloading, and **d** four-side fast unloading

significantly enhanced, indicating that a large number of microcracks caused by unloading appeared in the sandstone during the rapid unloading stage. In paragraph (c), the increase of  $\Delta\alpha$  from single-face unloading to four-face unloading is: 6%, 9%, 12% and 16%; the decrease of  $\Delta f(\alpha)$  is: 57%, 78%, 93% and 105%. Enter to (d) section unloading is completed. As the axial stress continued to increase, a large number of microcracks appeared in the sandstone and gradually expanded and penetrated,  $\Delta\alpha$  showed a rapid upward trend, and  $\Delta f(\alpha)$  showed a rapid downward trend. In segment (e) near the burst point,  $\Delta\alpha$  and  $\Delta f(\alpha)$  show a slight decrease and increase, and then fluctuate rapidly to extreme values. Note that the stress–strain curve of the four-face unloaded rockburst has no yield stage (e), and  $\Delta\alpha$  and  $\Delta f(\alpha)$  do not show a drop and rise just before failure. In the post-peak stage, with the occurrence of rockburst, the stress decreases rapidly and the sandstone is destroyed, corresponding to the sudden drop and sudden

rise of  $\Delta\alpha$  and  $\Delta f(\alpha)$ , respectively. For sandstones with different NUS, the positions of  $\Delta\alpha$  sudden drop and sudden increase are also different. When the NUS is single-side, double-side, and three-side, the positions where  $\Delta\alpha$  drops sharply correspond to 95.3%, 97.6%, and 98.3% of the peak stress, respectively, while the positions where  $\Delta\alpha$  increases sharply are 95.8%, 97.6%, and 98.5%, respectively. Taking the changing trend of the multifractal parameter  $\Delta\alpha$  first suddenly drops and then suddenly rises as the precursor of rockburst, it can be found that the hysteresis of the precursor of rockburst increases with the increase of the NUS. There is almost no precursor information for the four-side unloading rockburst. During the loading process of rockburst with different NUS, the overall change trend of the multifractal parameters is the same, and the increase of the multifractal spectral width  $\Delta\alpha$  corresponds to the decrease of  $\Delta f(\alpha)$ .

## 4 Conclusions

In this paper, the rockburst simulation experiment with multiple free-face rock structures is carried through the self-developed true triaxial rockburst experimental apparatus that can realize multi-side fast unloading in the horizontal loading direction under high-stress out. The stress–strain curve, energy evolution, failure process, and AE of the experiment are analyzed, and the following main conclusions are obtained:

1. As the NUS increases, the confining pressure constraint decreases gradually, and the axial peak stress and strain decrease gradually. The increment of the axial strain of the rockburst at the fast unloading point increases with the increase of the NUS. We believe that the fast unloading of the true triaxial in the horizontal direction under high-pressure loading is equivalent to applying tensile stress in the unloading direction. The loaded sample will expand along the unloading direction, resulting in a sudden increase in axial strain.
2. The dissipated energy of the rockburst will increase suddenly during fast unloading, indicating that fast unloading will damage the rock. With the increase in the NUS, the total energy and elastic strain energy of axial stress at the peak point gradually decrease while the dissipated energy gradually increases. The difference between the total energy input by the rockburst system at the peak point and the total energy input by the system after the rockburst gradually decreases with the increase of the NUS, indicating that the sandstone shows more brittle failure characteristics. With the increase in the NUS, the release rate of elastic strain energy during rockburst increases, the rockburst becomes more intense, and the mass and thickness of the rockburst ejection fragment gradually increase.
3. The sudden increase of AE cumulative hits at the rockburst's fast unloading point increases with the NUS's increase, indicating that the number of cracks produced by unloading increases gradually. The multifractal spectrum width of the multi-side unloading rockburst is not the same, indicating differences in the microfracture characteristics of the rockburst evolution process. During fast unloading,  $\Delta\alpha$  increases and  $\Delta f(\alpha)$  decreases, and the multifractal features are apparent. The changing trend of the multifractal parameter  $\Delta\alpha$  suddenly drops and then rises as the precursor of rockburst. The hysteresis of the rockburst precursor increases with the NUS increase.

**Acknowledgements** This research was supported by the National Natural Science Foundation of China (Grant Nos. 41941018 and

52074299), Fundamental Research Funds for the Central Universities (Grant No. 2021JCCXSB03), and Program of China Scholarship Council (202006430049).

**Data availability** Data generated or analyzed during this study are available from the corresponding author upon reasonable request.

## Declarations

**Conflict of interest** The author(s) declared no potential conflicts of interest with respect to the research, authorship, and/or publication of this article.

## References

- Akdag S, Karakus M, Taheri A (2018) Effects of thermal damage on strain burst mechanism for brittle rocks under true-triaxial loading conditions. *Rock Mech Rock Eng* 51(6):1657–1682
- Bruning T, Karakus M, Akdag S (2018) Influence of deviatoric stress on rockburst occurrence: an experimental study. *Int J Min Sci Technol* 28(5):763–766
- Cai MF, Wang J, Wang S (2001) Prediction of rock burst with deep mining excavation in Linglong gold mine. *Int J Min Met Mater* 8(4):241–243
- Chen ZY, Su GS, Ju J (2019) Experimental study on energy dissipation of fragments during rockburst. *B Eng Geol Environ* 78(7):5369–5386
- Cook NGW (1963) The basic mechanics of rockbursts. *J S Afr I Min Metall* 64(3):71–81
- Das R, Singh TN (2022) A novel technique for temporal evolution of rockburst in underground rock tunnel: an experimental study. *Environ Earth Sci* 81(17):420
- Esterhuizen GS, Dolinar DR, Ellenberger JL (2011) Pillar strength in underground stone mines in the United States. *Int J Rock Mech Min* 48(1):42–50
- Fakhimi A, Hosseini O, Theodore R (2016) Physical and numerical study of strain burst of mine pillars. *Comput Geotech* 74:36–44
- Fan PX, Li Y, Zhao YT (2018) Experimental study on unloading failure strength of red sandstone. *Chin J Rock Mech Eng* 37:852–861 (in Chinese)
- Feng XT, Liu J, Chen B (2017) Monitoring, warning, and control of rockburst in deep metal mines. *Engineering* 3(4):538–545
- Gercek H (2007) Poisson's ratio values for rocks. *Int J Rock Mech Min* 44(1):1–13
- Gong FQ, Wang Y, Wang Z (2021) A new criterion of coal burst proneness based on the residual elastic energy index. *Int J Min Sci Technol* 31(4):553–563
- Gong FQ, Ni Y, Ren L (2022) Effects of loading rate on rockburst proneness of granite from energy storage and surplus perspectives. *Rock Mech Rock Eng* 55(10):6495–6516
- Gu JC, Fan J, Kong FL (2014) Mechanism of ejective rockburst and model testing technology. *Chin J Rock Mech Eng* 33(6):1081–1089 (in Chinese)
- He MC, Miao JL, Feng JL (2010) Rock burst process of limestone and its acoustic emission characteristics under true-triaxial unloading conditions. *Int J Rock Mech Min* 47(2):286–298
- He MC, Nie W, Zhao ZY (2012) Experimental investigation of bedding plane orientation on the rockburst behavior of sandstone. *Rock Mech Rock Eng* 45(3):311–326
- He MC, Liu DQ, Gong WL (2014) Development of a testing system for impact rockbursts. *Chin J Rock Mech Eng* 33(9):1729–1739 (in Chinese)

- He MC, Ren FQ, Liu DQ (2018) Rockburst mechanism research and its control. *Int J Min Sci Technol* 28(5):829–837
- He MC, Li JY, Ren FQ (2020) Rock burst criterion based on clay mineral content. *Arab J Geosci* 13(4):1–8
- He MC, Li JY, Liu DQ (2021a) A novel true triaxial apparatus for simulating strain bursts under high stress. *Rock Mech Rock Eng* 54(2):759–775
- He MC, Ren FQ, Liu DQ (2021b) Experimental study on strain burst characteristics of sandstone under true triaxial loading and double faces unloading in one direction. *Rock Mech Rock Eng* 54(1):149–171
- Kaiser PK, Yazici S, Maloney S (2001) Mining-induced stress change and consequences of stress path on excavation stability—a case study. *Int J Rock Mech Min* 38(2):167–180
- Kong B, Wang E, Li Z (2016) Nonlinear characteristics of acoustic emissions during the deformation and fracture of sandstone subjected to thermal treatment. *Int J Rock Mech Min* 90:43–52
- Kong X, Wang E, He X (2017) Time-varying multifractal of acoustic emission about coal samples subjected to uniaxial compression. *Chaos Solitons Fractals* 103:571–577
- Lee M, Song JW, Park JH (2017) Asymmetric multi-fractality in the U.S. stock indices using index-based model of A-MFDFA. *Chaos Solitons Fractals* 97:28–38
- Li XB, Gong FQ, Tao M (2017) Failure mechanism and coupled static-dynamic loading theory in deep hard rock mining: a review. *J Rock Mech Geotech* 9(4):767–782
- Liu J, Wang EY, Li ZH (2013) Multi-fractal characteristics of surface potential of coal during the fracture. *J China Coal Soc* 38(9):1616–1620
- Lu WB, Yang J, Yan P (2012) Dynamic response of rock mass induced by the transient release of in-situ stress. *Int J Rock Mech Min* 53:129–141
- Ortlepp WD, Stacey TR (1994) Rockburst mechanisms in tunnels and shafts. *Tunn Undergr Sp Tech* 9(1):59–65
- Qiu SL, Feng XT, Xiao JQ (2014) An experimental study on the pre-peak unloading damage evolution of marble. *Rock Mech Rock Eng* 47(2):401–419
- Ren FQ, Zhu C, He MC (2020) Moment tensor analysis of acoustic emissions for cracking mechanisms during schist strain burst. *Rock Mech Rock Eng* 53(1):153–170
- Si XF, Gong FQ (2020) Strength-weakening effect and shear-tension failure mode transformation mechanism of rockburst for fine-grained granite under triaxial unloading compression. *Int J Rock Mech Min* 131:104347
- Stacey TR (2016) Addressing the consequences of dynamic rock failure in underground excavations. *Rock Mech Rock Eng* 49(10):4091–4101
- Steif PS (1984) Crack extension under compressive loading. *Eng Fract Mech* 20(3):463–473
- Su GS, Jiang J, Feng X (2019) Influence of loading rate on strainburst: an experimental study. *B Eng Geol Environ* 78(5):3559–3573
- Wang JA, Park HD (2001) Comprehensive prediction of rockburst based on analysis of strain energy in rocks. *Tunn Undergr Sp Tech* 16(1):49–57
- Wang GL, Zhang L, Xu M (2019) Energy damage evolution mechanism of non-across jointed rock mass under uniaxial compression. *Chin J Geotech Eng* 41(4):639–647 (in Chinese)
- Wang CL, He BB, Hou XL (2020) Stress-energy mechanism for rock failure evolution based on damage mechanics in hard rock. *Rock Mech Rock Eng* 53(3):1021–1037
- Wang CL, Cao C, Liu Y (2021) Experimental investigation on synergistic prediction of rockburst using the dominant-frequency entropy of acoustic emission. *Nat Hazards* 108(3):3253–3270
- Wibisono DY, Arora K, Majumder D (2023) Laboratory-scale rockburst physical model testing using a true-triaxial cell. *IOP Conf Ser Earth Environ Sci* 1124(1):012039
- Xie HQ, He CH (2004) Study of the unloading characteristics of a rock mass using the triaxial test and damage mechanics. *Int J Rock Mech Min* 41:74–80
- Xiong G, Yu W, Xia W (2016) Multifractal signal reconstruction based on singularity power spectrum. *Chaos Solitons Fractals* 91:25–32
- Yang SQ, Tian WL, Elsworth D (2020) An experimental study of effect of high temperature on the permeability evolution and failure response of granite under triaxial compression. *Rock Mech Rock Eng* 53(10):4403–4427
- Yu W, Wu G, Pan B (2021) Experimental investigation of the mechanical properties of sandstone-coal-bolt specimens with different angles under conventional triaxial compression. *Int J Geomech* 21(6):04021067
- Zhang YB, Yu GY, Tian BZ (2017) Experimental study of acoustic emission signal dominant-frequency characteristics of rockburst in a granite tunnel. *Rock Soil Mech* 38(5):1258–1266 (in Chinese)
- Zhang L, Zhang X, Wu J (2020) Rockburst prediction model based on comprehensive weight and extension methods and its engineering application. *B Eng Geol Environ* 79(9):4891–4903
- Zhao K, Yu X, Zhou Y (2020) Energy evolution of brittle granite under different loading rates. *Int J Rock Mech Min* 132:104392
- Zhou ZL, Cai X, Li X (2020) Dynamic response and energy evolution of sandstone under coupled static-dynamic compression: insights from experimental study into deep rock engineering applications. *Rock Mech Rock Eng* 53(3):1305–1331

**Publisher's Note** Springer Nature remains neutral with regard to jurisdictional claims in published maps and institutional affiliations.

Springer Nature or its licensor (e.g. a society or other partner) holds exclusive rights to this article under a publishing agreement with the author(s) or other rightsholder(s); author self-archiving of the accepted manuscript version of this article is solely governed by the terms of such publishing agreement and applicable law.